

# Ducted Assembly Steady-State Heat Transfer Software (DASSH)

---

*Theory Manual*

Nuclear Engineering Division

### **About Argonne National Laboratory**

Argonne is a U.S. Department of Energy laboratory managed by UChicago Argonne, LLC under contract DE-AC02-06CH11357. The Laboratory's main facility is outside Chicago, at 9700 South Cass Avenue, Argonne, Illinois 60439. For information about Argonne and its pioneering science and technology programs, see [www.anl.gov](http://www.anl.gov).

### **DOCUMENT AVAILABILITY**

**Online Access:** U.S. Department of Energy (DOE) reports produced after 1991 and a growing number of pre-1991 documents are available free at OSTI.GOV (<http://www.osti.gov/>), a service of the US Dept. of Energy's Office of Scientific and Technical Information.

### **Reports not in digital format may be purchased by the public from the National Technical Information Service (NTIS):**

U.S. Department of Commerce  
National Technical Information  
Service 5301 Shawnee Rd  
Alexandria, VA 22312  
**[www.ntis.gov](http://www.ntis.gov)**  
Phone: (800) 553-NTIS (6847) or (703) 605-6000  
Fax: (703) 605-6900  
Email: **[orders@ntis.gov](mailto:orders@ntis.gov)**

### **Reports not in digital format are available to DOE and DOE contractors from the Office of Scientific and Technical Information (OSTI):**

U.S. Department of Energy  
Office of Scientific and Technical Information  
P.O. Box 62  
Oak Ridge, TN 37831-0062  
**[www.osti.gov](http://www.osti.gov)**  
Phone: (865) 576-8401  
Fax: (865) 576-5728  
Email: **[reports@osti.gov](mailto:reports@osti.gov)**

### **Disclaimer**

This report was prepared as an account of work sponsored by an agency of the United States Government. Neither the United States Government nor any agency thereof, nor UChicago Argonne, LLC, nor any of their employees or officers, makes any warranty, express or implied, or assumes any legal liability or responsibility for the accuracy, completeness, or usefulness of any information, apparatus, product, or process disclosed, or represents that its use would not infringe privately owned rights. Reference herein to any specific commercial product, process, or service by trade name, trademark, manufacturer, or otherwise, does not necessarily constitute or imply its endorsement, recommendation, or favoring by the United States Government or any agency thereof. The views and opinions of document authors expressed herein do not necessarily state or reflect those of the United States Government or any agency thereof, Argonne National Laboratory, or UChicago Argonne, LLC.

# **Ducted Assembly Steady-State Heat Transfer Software (DASSH) – Theory Manual**

---

Prepared by  
Milos Atz, Micheal A. Smith, and Florent Heidet  
Nuclear Engineering Division, Argonne National Laboratory

August 6, 2021



## REVISION HISTORY

---

Name	Date	Reason for changes	Version
Milos Atz	2021-08-06	Initial preparation	0.0

---

## SUMMARY

The Ducted Assembly Steady-State Heat transfer software (DASSH) is being developed at Argonne National Laboratory to obtain a steady-state thermal fluids result for the coolant flow and temperature distribution in a hexagonally gridded reactor core with ducted assemblies. In DASSH, each assembly is assumed to contain a hexagonal bundle of wire-wrapped pins. DASSH divides the coolant in the pin bundle into subchannels on which it applies energy balances to determine coolant and duct temperatures. DASSH offers multiple models for inter-assembly heat transfer and features the ability to calculate pin temperatures.

This document describes the models and equations implemented in DASSH. It includes a description of the geometric system to which the models are applied and a derivation of the subchannel energy balance formulation is presented. It also reviews the available correlations and provides an overview of the process by which power distributions are generated. Finally, it covers the code execution procedure, discussing the main code objects and their interactions.

## TABLE OF CONTENTS

Revision History .....	i
Summary .....	ii
Table of Contents .....	iii
List of Figures .....	v
List of Tables .....	v
1 Introduction .....	1
2 Problem overview and system description .....	4
2.1 Problem overview .....	4
2.2 Description of system geometry .....	5
3 DASSH model and theory .....	11
3.1 Governing equation.....	11
3.2 Application to ducted assemblies.....	12
3.3 Region I: Interior subchannels .....	16
3.4 Region II: Edge and corner subchannels.....	19
3.5 Flowing bypass and inter-assembly gap coolant.....	24
3.6 Stagnant inter-assembly gap coolant models .....	27
3.6.1 Model 1: Conduction model.....	28
3.6.2 Model 2: Duct-average model .....	29
3.6.1 Energy balance error.....	29
3.7 Treating mesh disagreement in the inter-assembly gap .....	30
3.7.1 Projection of coarse wall temperatures to fine inter-assembly gap mesh.....	30
3.7.2 Restriction of fine inter-assembly gap temperatures to coarse wall mesh .....	33
3.8 Duct walls .....	36
3.9 Numerical stability and axial-mesh size requirements.....	38
3.10 Applicability of solution method .....	42
3.11 Pressure drop.....	43
3.12 Low-fidelity models .....	44
3.12.1 Model description .....	45
3.12.2 Approximating pin bundles with low-fidelity model .....	47
3.12.3 Combination of axial regions in an assembly .....	48
3.13 Convection approximation .....	49
3.14 Energy balance calculation .....	50
3.15 Pin temperatures .....	53
3.15.1 Coolant temperatures .....	53
3.15.2 Clad temperatures .....	53
3.15.3 Fuel surface temperature .....	55
3.15.4 Fuel temperatures .....	55
4 Review of correlations built into DASSH .....	60
4.1 Bundle friction factor .....	62
4.1.1 Novendstern (1972) .....	62

4.1.2	Rehme (1973) .....	63
4.1.3	Engel et al. (1979) .....	64
4.1.4	Cheng-Todreas Detailed (1986) .....	64
4.1.5	Cheng-Todreas Simple (1986) .....	68
4.1.6	Upgraded Cheng-Todreas (2018) .....	69
4.2	Flow split .....	70
4.2.1	Novendstern (1972) .....	70
4.2.2	MIT Chiu-Todreas-Rohsenow (1980) .....	70
4.2.3	Cheng-Todreas (1986) .....	72
4.3	Mixing parameters .....	72
4.3.1	Chiu, Rohsenow, and Todreas (1978) .....	73
4.3.2	Cheng-Todreas (1986) .....	73
4.4	Heat transfer coefficient .....	75
4.5	Fuel thermal conductivity .....	76
5	Power distributions .....	78
5.1	Obtaining power distributions from ARC: VARPOW .....	78
5.2	User-specified power distributions .....	80
6	DASSH code calculation procedure .....	82
6.1	Reading input, problem setup .....	83
6.2	Solution sweep procedure .....	85
6.3	DASSH output .....	87
7	Conclusions .....	89
8	References .....	90
Appendix A	Pin bundle dimension definitions .....	93



## LIST OF FIGURES

Figure 1. Dimensions and definitions applied to single-ducted assembly .....	6
Figure 2. Subchannel map for 61-pin bundle.....	7
Figure 3. Dimensions and definitions applied to double-ducted assembly.....	8
Figure 4. Pin-bundle indexing in DASSH .....	8
Figure 5. Assembly indexing in DASSH.....	9
Figure 6. Inter-assembly gap subchannel indexing in DASSH.....	10
Figure 7. Two-region model for coolant flow in hexagonal, ducted assembly with wire-wrapped pins. ....	14
Figure 8. Subchannel adjacency illustrations for interior-type subchannels. ....	17
Figure 9. Adjacencies for subchannels along the duct wall. ....	22
Figure 10. Inter-assembly gap and gap-corner subchannels in single-ducted assemblies	26
Figure 11. Example of possible disagreement in subchannel meshing between adjacent assemblies .....	30
Figure 12. Mesh disagreement between inter-assembly gap subchannel and two duct elements .....	31
Figure 13. Mesh disagreement between duct element and inter-assembly gap subchannels .....	34
Figure 14. Diagram of duct wall 1-D heat transfer model .....	37
Figure 15. Coolant and duct subchannels for the low-fidelity assembly model .....	45
Figure 16. Minimum lateral porosity as a function of pin bundle pitch-to-diameter ratio. ....	48
Figure 17. Diagram showing example combination of axial regions in an assembly.....	49
Figure 18. Diagram of fuel pellet shell model system .....	56
Figure 19. Diagram illustrating fuel temperature model radial noding .....	58
Figure 20. Organization of main code objects in DASSH.....	82
Figure 21. DASSH sweep algorithm flowchart .....	86

## LIST OF TABLES

Table 1. Summary of correlations built into DASSH and their ranges of applicability ...	61
Table 2. Polynomial factors for bare-rod friction factor constant correlation .....	67
Table 3. VARPOW material classification .....	79
Table 4. CSV structure for user-specified power distributions in DASSH.....	81
Table 5. Main DASSH objects relevant to code execution.....	82
Table 6. Description of summary output file tables .....	87



## 1 Introduction

A critical design requirement for power-producing systems is to ensure sufficient safety related thermal margins for all components. These margins may be adopted to protect against any number of possible heat-induced system failure modes, such as component melting, unintended coolant boiling, or thermal stress that leads to mechanical failure. Additionally, it is advantageous to balance the temperature profile of the system, thereby reducing the potential for thermal stripping and maximizing plant efficiency. To demonstrate that a system design meets margins and achieves reasonable thermal performance, designers must understand how heat is transferred throughout the system.

The Ducted Assembly Steady-State Heat transfer software (DASSH) is being developed at Argonne National Laboratory to obtain a steady-state thermal fluids for hexagonally gridded reactor cores with ducted assemblies. DASSH specifically calculates pressure drop in the assemblies and temperatures in the coolant, ducts, and pins based on an assigned coolant mass flow rate. DASSH is intended for use as part of the reactor design process to provide a rapid assessment of the flow and temperature distribution, especially when assembly designs are not fully developed. Because DASSH is built on an assumed geometry model and based on an intermediate-fidelity subchannel model, it is not expected to provide definitive flow and temperature solutions, but it does have the flexibility, via user input, to match the behavior of experimentally measured assembly designs.

DASSH divides each assembly into subchannels and an energy balance formulation is used to determine coolant temperatures. Assuming a steady-state solution exists for a given reactor configuration, DASSH uses correlated parameters for friction and turbulent mixing to avoid the need to solve the coupled energy and momentum equations. DASSH solves an approximate form of the energy conservation equation in which the dominant heat transfer mechanisms are modeled and secondary ones ignored to allow for a computationally inexpensive means to obtain the coolant temperature distribution. Codes such as DASSH are an important part of reactor design because they can generate intermediate-fidelity thermal-hydraulics (TH) results for the steady-state behavior with relatively inexpensive calculations.

DASSH is an alternative to the legacy TH code SE2-ANL [1]. In SE2-ANL, the SUPERENERGY-2 code [2] was directly interfaced with the Argonne Reactor Computational (ARC) code suite [3]. ARC provides the pin power distribution and SUPERENERGY-2 evaluates the coolant temperatures given the power distribution. SE2-ANL also includes a pin-level temperature calculation and reactor hot spot analysis method where both nominal and two-sigma temperatures are calculated using the semi-statistical method [4]. DASSH is intended to be a rebuild of the SE2-ANL capability and thus preserve all of the SE2-ANL capabilities while improving accuracy, usability, and sustainability. DASSH has the following improvements over SE2-ANL:

- In DASSH, the convective heat transfer between duct walls and coolant can be modeled explicitly based on duct wall surface temperatures, whereas SE2-ANL employs a lumped thermal resistance between the coolant and the duct mid-wall temperature.
- DASSH features an improved model for double-ducted assemblies in which the two duct walls and the bypass gap between them are modeled explicitly. By contrast, in SE2-ANL, the inner duct was ignored and the flow rate to the pin bundle was reduced to 75% of the assigned value.
- DASSH updates material properties and correlated parameters at every axial step, whereas SE2-ANL uses material properties evaluated at a single average temperature for the whole core.
- The power distribution from neutron and gamma heating is obtained from DIF3D-VARIANT [5] whereas SE2-ANL uses DIF3D-FD [6] with a restriction on the triangular meshing. DASSH eliminates the SE2-ANL assumption that the radial pin power distribution in each assembly does not change axially. In DASSH, the axial power shape for each pin is obtained via the evaluation of the DIF3D-VARIANT basis functions. DASSH distributes neutron and gamma heating to the fuel, cladding, ducts, and coolant based upon the reaction rate distribution whereas SE2-ANL only allowed heating of the fuel and, optionally, gamma heating of the duct.

- With DASSH, users can assign different structural material properties in each assembly. Additionally, users may select from different built-in correlations beyond those available in SE2-ANL. DASSH can be extended to handle other coolant types (e.g. lead or molten salt) by including the coolant properties and adding different correlations as necessary, whereas this is not practical in SE2-ANL.
- DASSH eliminates the SE2-ANL assumption of a pin-lattice geometry throughout the modeled axial domain by allowing users to specify porous body medium input for low importance regions. This feature is particularly useful for early in the reactor design process where many parts of the reactor design might not yet be defined.
- To take advantage of the extensive data it generates, DASSH includes visualization capabilities on the pin, subchannel, and assembly levels.
- DASSH offers significant improvements in usability and maintainability over SE2-ANL. DASSH is written in Python 3 following software development best practices. The input and output are clearer than SE2-ANL and the code rigorously checks user input for mistakes.

This theory manual describes the DASSH code and the heat transfer models that it evaluates. Section 2 describes the problem to be solved and defines the system geometry and key parameters. Section 3 provides a description of the model and heat transfer methodology while Section 4 discusses the correlations for flow and heat transfer parameters that DASSH uses. Section 5 describes the pathways by which DASSH obtains power distributions from ARC binary files or user input. Section 6 covers the code structure of DASSH and outlines the execution procedure.

Descriptions of the installation procedure, input file formatting, and output file generation and processing are provided in the DASSH User Guide [7]. A report on DASSH benchmarking against experiment and other simulations is in preparation. Further documentation may be produced in the future as DASSH undergoes verification and validation.

## 2 Problem overview and system description

This chapter describes the type of problem to be solved by DASSH. This document aims to provide a more comprehensive description of the system and its connection to the theory discussed in later sections than is available in existing literature.

### 2.1 Problem overview

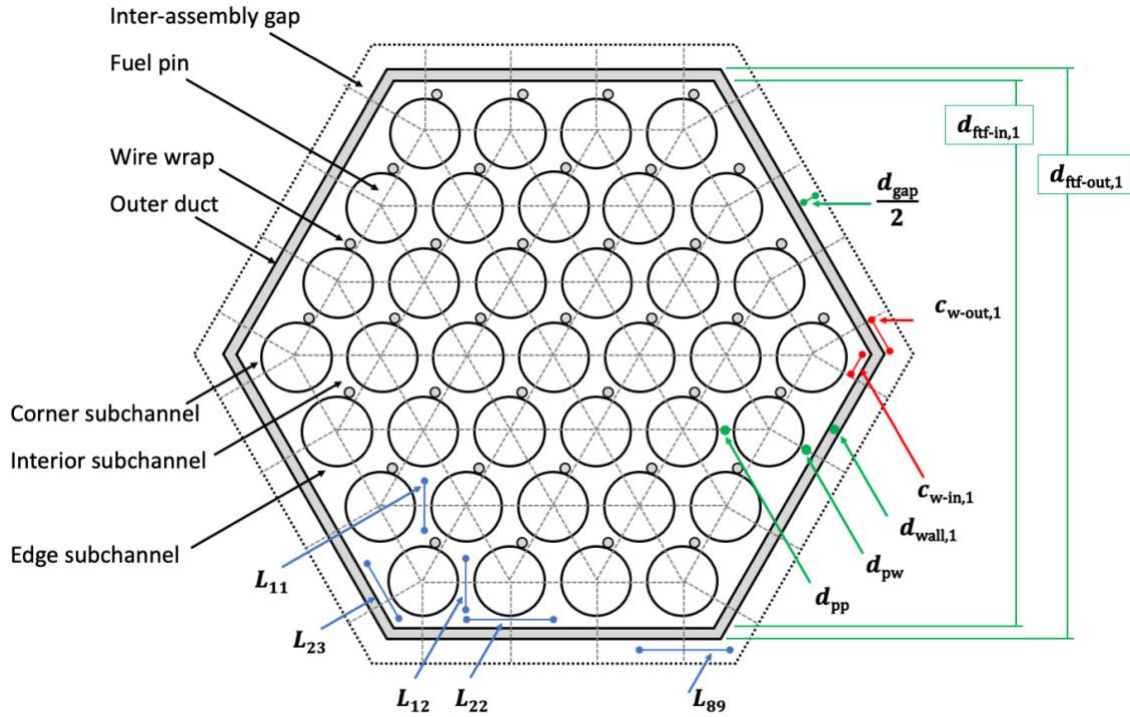
DASSH is developed for incompressible, steady-state thermal fluids analysis in reactor cores made up of ducted, hexagonal assemblies. By conservation of energy at steady state, all heat generated in the system is removed by the coolant. The bulk coolant inlet temperature is user input along with the assignment of coolant mass flow rate in each assembly or the coolant temperature change over an assembly. Power is defined as a series of axial power (W/m) profiles for each pin and duct and coolant subchannel mesh. The axial power profiles for a given assembly are simple polynomial functions and can be provided as user input. Alternatively, the same power distribution can be computed internally in DASSH by taking binary files from a GAMSOR [8] execution. Given the inlet temperature, power distribution, and coolant mass flow rate, DASSH can calculate the coolant and duct temperatures throughout the core.

Within each ducted assembly, heat is transferred axially by assuming forced advection. Radially, between sub-channels interior to the duct, the system is connected by a modified conduction term. This modified conduction term is used to account for the turbulent mixing of coolant and is based upon correlations related to the geometry and flow rate. Heat is transferred between the coolant and the duct via convection and through the duct wall via conduction. DASSH uses an axial forward-difference marching scheme, meaning that the coolant temperatures at each axial plane are only dependent on the temperatures in the preceding plane and power generation in the current plane. The duct wall temperatures at each axial plane are lagged by one plane with respect to the coolant temperatures to decouple each assembly and avoid the need for a core-wide solution algorithm. The forward-difference marching scheme is simple, but it introduces an axial mesh size constraint that must be met to guarantee numerical stability.

## **2.2 Description of system geometry**

DASSH is developed for incompressible, steady-state thermal fluids analysis in reactor cores made up of ducted, hexagonal assemblies. Each assembly contains a pin bundle arranged in a hexagonal lattice. The pins are wrapped with wire to preserve spacing and promote mixing. As is done in numerical modeling of thermal fluids for other types of reactors and assemblies, DASSH divides the computational model of each assembly into subchannels. This section defines these subchannels and other geometric quantities important to the derivation of the equations implemented in DASSH. Figure 1 displays the basic ducted hexagonal assembly geometry assuming a single duct wall. The definitions of the various geometric lengths displayed in Figure 1 are provided in Appendix A.

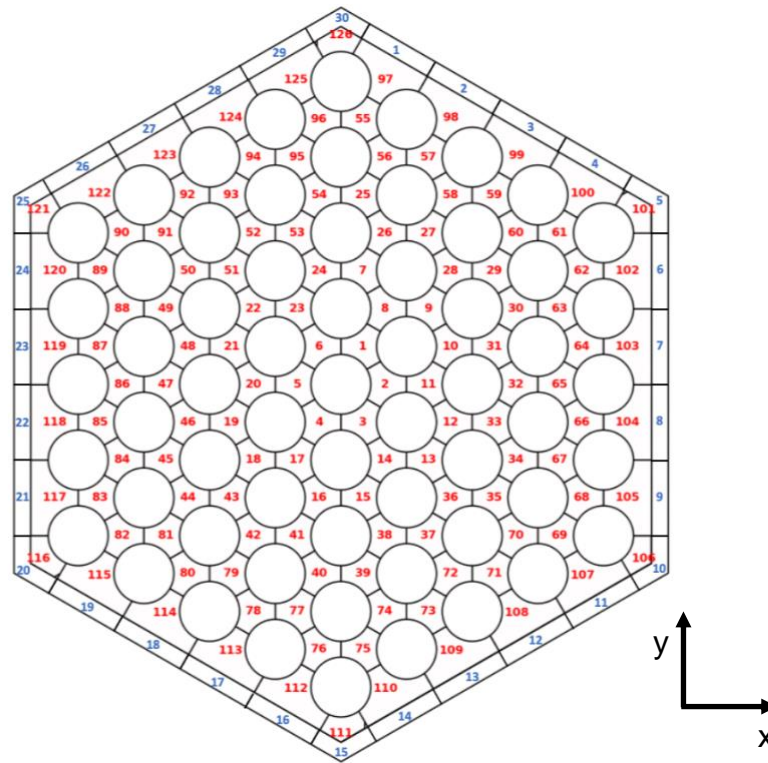
The region within the innermost duct, in which the pin bundle is located, is referred to hereafter as the assembly interior. As shown in Figure 1, at most three types of coolant subchannels exist in the assembly interior. The interior subchannels (Type 1) sit between three pins. Each interior subchannel mesh is connected to three other subchannels with only two distinct connection types (either to an interior or edge subchannel). The edge subchannels (Type 2) are located between pins next to the duct wall. Each edge subchannel mesh is always connected to three subchannels with three possible configurations: 1) two edge and one interior channel; 2) one edge, one corner, and one interior channel; and 3) two corner and one interior channel. The corner subchannels (Type 3) only intersect a single pin and contact no interior subchannels. Each corner subchannel is connected to two corner subchannels (one-pin geometry case) or two edge subchannels (in assemblies with 7 or more pins). For the 37-pin assembly shown in Figure 1, there are 54 interior channels, 18 edge channels, and 6 corner channels, resulting in a total of 78 subchannels in the assembly-interior coolant region. In addition to the coolant subchannel types, there are two types of duct wall elements: edges and corners.



**Figure 1. Dimensions and definitions applied to single-ducted assembly**

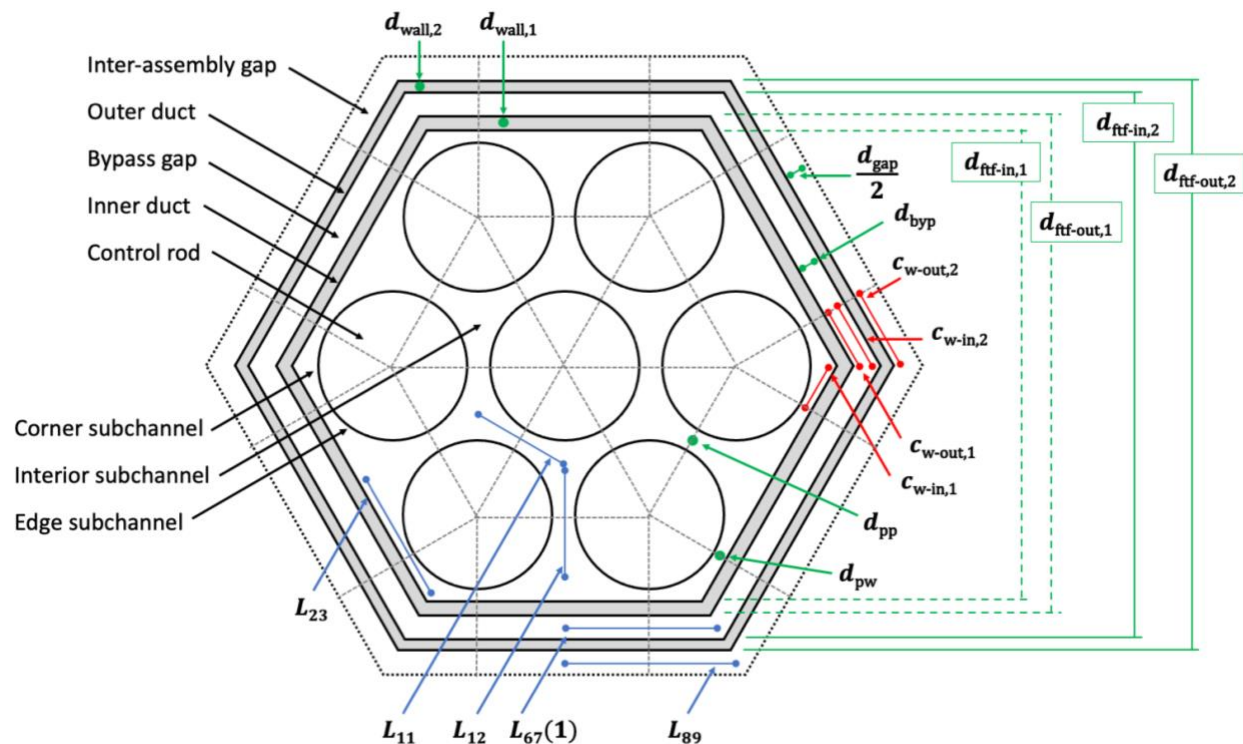
Figure 2 shows the indexing of coolant subchannels and ducts in DASSH. The coolant subchannels are labeled in red and the duct elements are labeled in blue. The lines that occupy the coolant region denote the boundaries of the subchannels. Pins are shown as white circles. The indexing counts subchannels in clockwise rings, starting from the ring of subchannels that surrounds the centermost pin. All interior-type (Type 1) subchannels are indexed before edge (Type 2) and corner (Type 3) subchannels. All coolant subchannels are indexed before duct elements, which are indexed by continuing the clockwise rotation around the assembly. Note that each edge and corner coolant subchannel interfaces with only one duct surface.





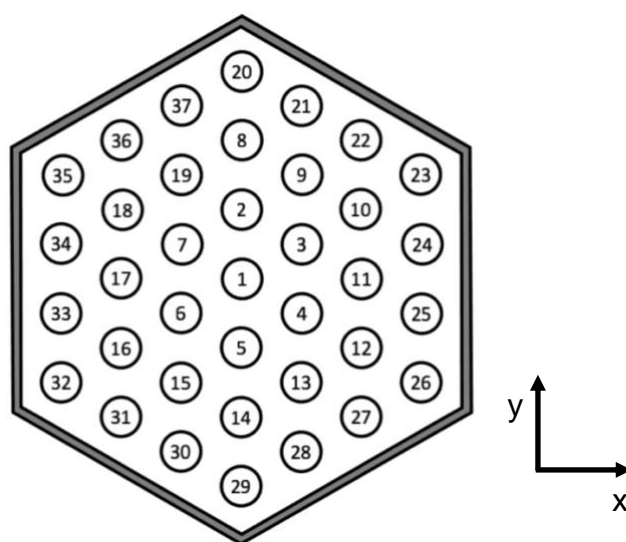
**Figure 2. Subchannel map for 61-pin bundle**

Figure 3 displays a double-ducted assembly in which some coolant within the assembly is diverted into a gap between an inner and outer duct wall. Such a design is generally used for control assemblies. The ducts are counted beginning from the innermost duct and proceeding outward. The bypass gap between the ducts is comprised of edge and corner subchannels, which are defined as Types 6 and 7, respectively. The number of subchannels in the bypass gap and the number of elements in the duct wall are identical. Each bypass gap subchannel connects to two duct wall elements: one on the inner duct and one on the outer duct. These types of assemblies typically have a single orifice and the flow split between the duct bypass and the interior pin bundle is designed as part of the assembly orifice strategy.



**Figure 3. Dimensions and definitions applied to double-ducted assembly**

The pins in the bundle are arranged in a hexagonal lattice and are counted from the inside to outside in clockwise fashion around each hexagonal ring. The indexing for a 37-pin bundle is shown in Figure 4.



**Figure 4. Pin-bundle indexing in DASSH**

The assemblies are arranged in a hexagonal lattice where the indexing begins with the centermost assembly and counts the assemblies in each subsequent ring in a counterclockwise direction, as shown in Figure 5.

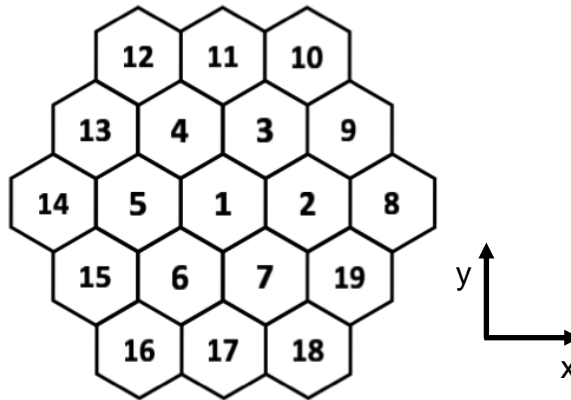


**Figure 5. Assembly indexing in DASSH**

Coolant also exists between the assemblies, outside of the outermost duct. This region is referred to as the inter-assembly gap. The inter-assembly gap is divided into edge and corner subchannels. Each edge subchannel connects to two assemblies and two adjacent gap subchannels. Each corner subchannel connects to three assemblies and three adjacent gap subchannels. Figure 6 shows how inter-assembly gap coolant subchannels are indexed for the first three assemblies assuming Assemblies 1 and 2 have three rings of pins (19 pins total) and Assembly 3 has two rings of pins (7 pins total). The subchannels in the pin-bundle region of Assemblies 2 and 3 are shown to highlight how the inter-assembly gap depends on the geometry of the adjacent assemblies. A diagram of the edge and corner subchannel geometry for two of the gap subchannels (indexed 3 and 4) is shown. The red numbers show the order of the hex faces. The subchannels are counted in rings around each assembly in the order seen in Figure 5. For each assembly, the gap subchannel index starts at Face 1 and fills in as-of-yet unindexed gap subchannels moving clockwise around the assembly hex faces. The inter-assembly gap is meshed to have the same number of edge and corner subchannels as the adjacent assembly with the most pins.

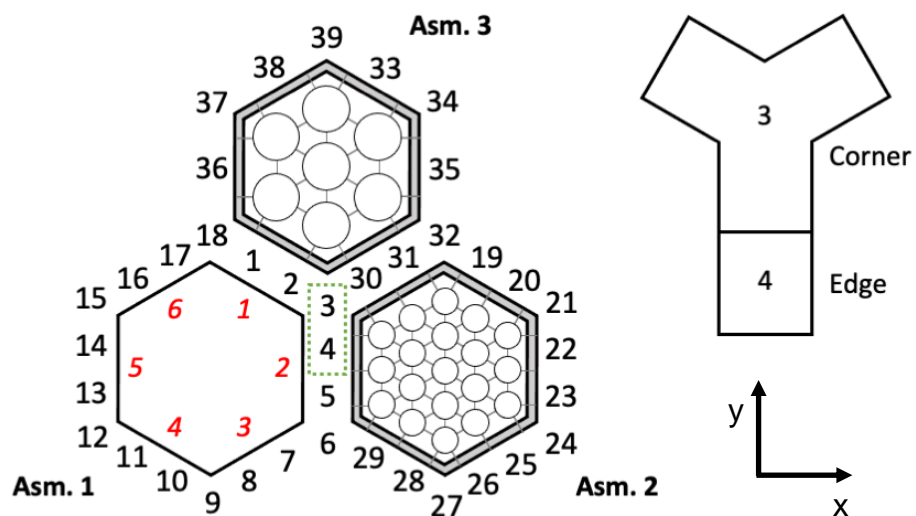


Figure 6. Inter-assembly gap subchannel indexing in DASSH

### 3 DASSH model and theory

This section presents the model, equations, and methodology applied in DASSH. The methodology is very similar to the one utilized in SUPERENERGY-2. The derivation presented in this section makes an explicit connection between the governing equation for energy conservation, the energy balance equations implemented in the model, and the assumptions required to reach them.

This chapter is organized as follows. Sections 3.1-3.10 derive the subchannel methodology, present the equations used to calculate temperatures in different types of subchannels, cover the axial mesh size constraint in each type of subchannel, and quantify the applicability of the forced convection assumption. Section 3.11 covers the calculation of pressure drop, Sections 3.12-3.13 introduce two simplified methods built into DASSH, Section 3.14 describes the calculation of the energy balance in DASSH used to check the energy conservation, and Section 3.15 discusses the calculation of pin temperatures.

#### 3.1 Governing equation

DASSH is based on the conservation of energy. Energy is conserved in every axial plane of the core. Conservation of any property  $\phi$  within a control volume can be expressed:

$$\frac{\partial \phi}{\partial t} + \nabla \cdot (\phi \vec{u}) + s = 0, \quad (3-1)$$

where:  $\vec{u}$  = velocity vector  
 $s$  = sources and sinks within control volume

The terms of Equation 3-1 can be summarized as shown in Equation 3-2.

$$\left[ \begin{array}{c} \text{Change in} \\ \phi \text{ over time} \end{array} \right] + \left[ \begin{array}{c} \text{Gain and loss of } \phi \\ \text{through boundaries} \end{array} \right] + \left[ \begin{array}{c} \text{Sources or sinks} \\ \text{in the system} \end{array} \right] = 0. \quad (3-2)$$

For energy,  $\phi = \rho h(\vec{r}, t)$ , where  $h$  is the specific enthalpy with units of heat per mass. Evaluation of Equation 3-1 for energy yields the following:

$$\frac{\partial \rho h}{\partial t} + \nabla \cdot (\rho h \vec{u}) = q''' + \psi + \nabla \cdot \rho \alpha \nabla h + \left[ \begin{array}{c} \text{Compressible} \\ \text{fluid terms} \end{array} \right]. \quad (3-3)$$

where:  $\rho$  = velocity vector  
 $h$  = energy sources and sinks within control volume  
 $q'''$  = volumetric heat generation (W/m<sup>3</sup>)  
 $\psi$  = work done against viscous forces (W/m<sup>3</sup>)  
 $\alpha$  = fluid thermal diffusivity (m<sup>2</sup>/s)

The terms on the left-hand side (LHS) are the change in control volume energy over time and the gain or loss of energy across control volume boundaries. The first three terms on the right-hand side (RHS) are an expansion of control volume energy sources and sinks, including volumetric internal heat generation, work done against viscous forces, and conduction through the control volume.

### 3.2 Application to ducted assemblies

Solving this differential equation using numerical methods requires solving the coupled transport equations for energy and momentum to find the flow into and out of the control volume. Although this is possible, it is computationally intensive. To avoid this, simplifying assumptions are applied to Equation 3-3. These assumptions require a conceptual discussion of fluid and heat flow in ducted assemblies typical of liquid metal fast reactors.

The standard subchannel model approach is to assign each subchannel its own degree of freedom set at each axial plane surface and define finite difference relationships between two adjacent planes and the radially connected subchannels. The geometric mapping involved in creating this system was the focus of Section 2. Power may be added to the system via the pins, the duct, or by direct heating of the coolant. Each subchannel internal to the duct has energy contributions from the adjacent pins based on a uniform heat flux such that the energy delivered to each subchannel depends only on the connected surface area with the adjacent pins. The interior and corner subchannels each get 1/6 of the power produced by each adjacent pin, whereas edge subchannels get 1/4 of the power from each adjacent pin. Additional power can be added to the coolant from direct heating. No power is assumed to be deposited in the inter-assembly gap coolant or in the bypass coolant between ducts in double-ducted assemblies.

In an assembly in which the coolant is under forced convection, the dominant modes of heat transfer are (1) axial advection due to coolant flow, (2) radial conduction through the coolant and (3) radial thermal mixing caused by turbulence due to the wire-wrap. Heat conduction through pins that would connect subchannels that do not have a fluid boundary is neglected. Similarly, heat is not conducted through the wire wrap. The presence of the wire-wrap and the duct surrounding the assembly causes two distinct flow regimes in the radial plane, as shown in Figure 7. In the interior of the assembly, Region I, the wire-wrap causes the coolant to spiral around the pins. At the bundle periphery next to the duct, Region II, the wire-wrap causes circulating flow in the direction of the wire around the entire assembly along the duct wall [9].

Based on this description of the system, the assumptions that DASSH applies to Equation 3-3 are summarized below.

1. Incompressible, frictionless coolant (the viscous and compressible terms in the energy equation are ignored) .
2. Steady-state condition exists.
3. Homogeneous, isotropic fluid properties.
4. No heat conduction in the axial direction (heat transfer in the axial direction occurs primarily by advection due to forced convection).
5. Gravitational forces in the energy equation are ignored as the fluid is subject to forced axial advection.
6. Advective heat transfer in the radial plane is ignored; instead, heat transfer from radial mixing under turbulent flow is lumped into the conduction term and approximated by enhancing the thermal diffusivity with an eddy diffusivity obtained from correlation.

Applying assumptions 1-3 to Equation 3-3 yields Equation 3-4, in which the time-derivative has been eliminated and material properties have been removed from the derivatives. Assuming that the heat capacity is constant, the enthalpy  $h$  can be replaced with  $C_p T$ , as shown.

$$\rho C_p \nabla \cdot (T \vec{u}) = q''' + \rho C_p \alpha \nabla \cdot \nabla T. \quad (3-4)$$

where:  $T$  = temperature (K)  
 $C_p$  = heat capacity (J/kgK)

DASSH accounts for enhanced radial mixing phenomena by using correlations. These correlations are reported for different assemblies with varying number of pins as functions of pin pitch, diameter, wire-wrap lead (the “wavelength” of the wrap, i.e. the axial distance along the pin for the wire to make one full wrap), and flow characteristics (Reynolds number, Re). An overview of the correlations available in DASSH is given in Section 4.

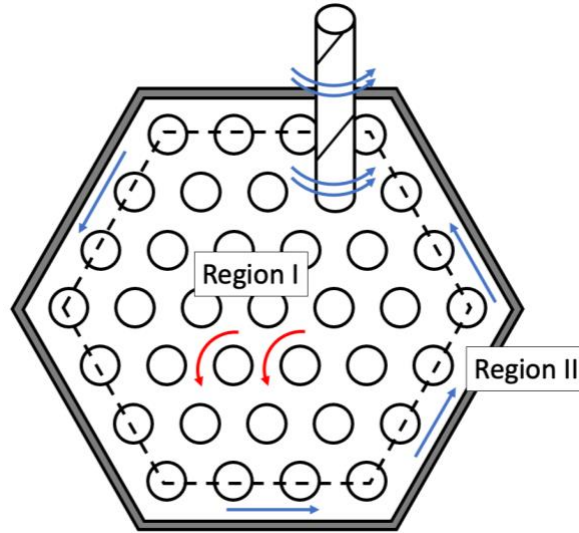


**Figure 7. Two-region model for coolant flow in hexagonal, ducted assembly with wire-wrapped pins.**

In Region I, the increase in radial mixing is modeled by an enhanced eddy diffusivity [10]. The eddy diffusivity augments the coolant thermal diffusivity. In this way, radial convection is being treated through correlation as enhanced radial conduction and the radial advection component of Term 2 on the LHS of Equation 3-4 is reduced to the axial direction only. For assemblies with wire-wrapped pins, the enhanced thermal diffusivity is given as Equation 3-5, which replaces the unmodified value of  $\alpha$  in Equation 3-4.



$$\alpha^* = \frac{\kappa k}{\rho C_p} + \varepsilon \quad (3-5)$$

where:  $k$  = fluid thermal conductivity (W/m-K)  
 $\kappa$  = conduction shape factor  
 $C_p$  = fluid specific heat (J/kg-K)  
 $\varepsilon$  = eddy diffusivity (m<sup>2</sup>/s)

The first term is the thermal diffusivity of the fluid itself ( $\alpha = k/\rho C_p$ ), with  $k$  as the thermal conductivity. It is assumed that heat is not transferred between coolant channels through the pins. This term is multiplied by a conduction shape factor, which may be specified by the user or based on a geometry-dependent correlation. The shape factor can be used to boost or suppress heat transfer as desired. The second term is the eddy diffusivity. The enhanced thermal diffusivity in Equation 3-5 can be expressed as an enhanced thermal conductivity by multiplying through by density and heat capacity, as shown in Equation 3-6.

$$k^* = \kappa k + \rho C_p \varepsilon \quad (3-6)$$

Depending on the state of flow in the assembly, the eddy diffusivity term can be over an order of magnitude greater than the conduction term. For pin bundles without wire wrap,  $\varepsilon = 0$ , meaning there is no enhancement of the conductivity even though turbulent mixing may still be occurring. Future work may require the development and implementation of new correlations to account for enhanced conductivity due to turbulent mixing in bundles without wire wrap.

In Region II, circumferential flow is driven by the synchronized sweeping of flow around the wire wrap. This is described by a swirl velocity, which is measured in correlations as the ratio between the circumferential and bundle average axial velocities. If the pins do not have wire wrap – a possibility for lower-power assemblies such as reflectors and shields – the swirl velocity is zero.

In the following subsections, the equations describing energy transfer in Regions I and II are derived from Equation 3-4 using the dimensions and definitions shown in Figure 1 and Figure 3 and described in Appendix A. Then, the equations for energy transfer in the bypass

gap, inter-assembly gap, and duct walls, and are presented in Sections 3.5-3.8. At the end of each subsection, the energy balance equations for each type of subchannel mesh are summarized. Because DASSH relies on an explicit axial-marching scheme (forward-difference), an axial-mesh size limit is needed to preserve numerical stability. The stability criteria are different for each type of subchannel and are presented in Section 3.9.

### 3.3 Region I: Interior subchannels

Equation 3-7 describes heat transfer in an interior subchannel  $i$  and is the result of applying the aforementioned assumptions to Equation 3-4. The terms for the time-dependence, for work done by viscous forces, and for compressible fluids have been dropped. From the Material properties (density,  $\rho$ , and thermal diffusivity,  $\alpha^*$ ) were pulled out from the derivatives. The flow of heat by advection has been reduced to the axial dimension. As discussed above, thermal mixing in the x-y directions is handled by using a modified thermal diffusivity  $\alpha^*$ , which includes both the standard thermal diffusivity of the fluid and the eddy diffusivity that accounts for radial mixing. In Equation 3-7, the enhanced thermal diffusivity is substituted with the enhanced thermal conductivity, obtained by multiplying through by density and heat capacity.

$$\rho C_p v_{i,z} \frac{\partial T_i}{\partial z} = q_i''' + k^* \nabla_{xy} \cdot \nabla_{xy} T_i. \quad (3-7)$$

where:  $v_{i,z}$  = axial velocity (m/s) in subchannel  $i$   
 $q_i'''$  = volumetric power (W/m<sup>3</sup>) added to subchannel  $i$

In Equation 3-7, there is no radial dependence of  $T$  on fluid flow, and therefore no requirement to solve the momentum transport equations. The system has been collapsed into a single solvable quantity. Each term has units of power (W) per volume. On the LHS,  $v_{1,z}$  is the velocity in the axial direction for interior subchannels, defined as the volumetric flow rate divided by the cross-sectional area in the x-y-plane. The right-hand side of Equation 3-7 may be viewed as a modified form of the heat equation. The Laplace operator in the second term on the RHS can be evaluated by taking the volume integral of Equation 3-7 (shown in Equation 3-8) and applying the divergence theorem, which dictates that the heat sources and sinks within

a control volume can be described by the rate at which heat flows into and out of the control volume. The result of this step is shown in Equation 3-9, of which the last term is a surface integral that describes the total heat flow into and out of the control volume.

$$\rho C_p \int_V v_{i,z} \frac{\partial T_i}{\partial z} dV = \int_V q_i''' dV + k^* \int_V \nabla_{xy} \cdot \nabla_{xy} T_i dV. \quad (3-8)$$

$$\rho C_p v_{i,z} V_i \frac{\partial T_i}{\partial z} = q_i + k^* \int_S \nabla_{xy} T_i \cdot n dS. \quad (3-9)$$

where:  $q_i$  = power (W) added to subchannel  $i$   
 $V_i$  = volume (m<sup>3</sup>) of subchannel  $i$

Each term in the above equations has units of power. The second term on the RHS of Equation 3-9 is equal to the net heat flux through the surfaces of the subchannel that connect to the other subchannels in the same plane. In Equation 3-10, that term is discretized radially into a summation of energy transferred between subchannel  $i$  and its three neighbors, which are displayed in Figure 8 for each type of subchannel adjacency. The indices  $A, B, C$  denote the subchannels adjacent to subchannel  $i$ . In Equation 3-10, the heat flux is evaluated at the interfaces between the mesh cells, which have cross-sectional area  $A_{A,i}$ ,  $A_{B,i}$ , and  $A_{C,i}$ , respectively. The far-right diagram in Figure 8 highlights the interface area through which heat transfer between interior subchannels occurs.

$$\int_S \nabla_{xy} T_i \cdot n dS = A_{A,i} \left. \frac{\partial T}{\partial r} \right|_{A,i} + A_{B,i} \left. \frac{\partial T}{\partial r} \right|_{B,i} + A_{C,i} \left. \frac{\partial T}{\partial r} \right|_{C,i}. \quad (3-10)$$

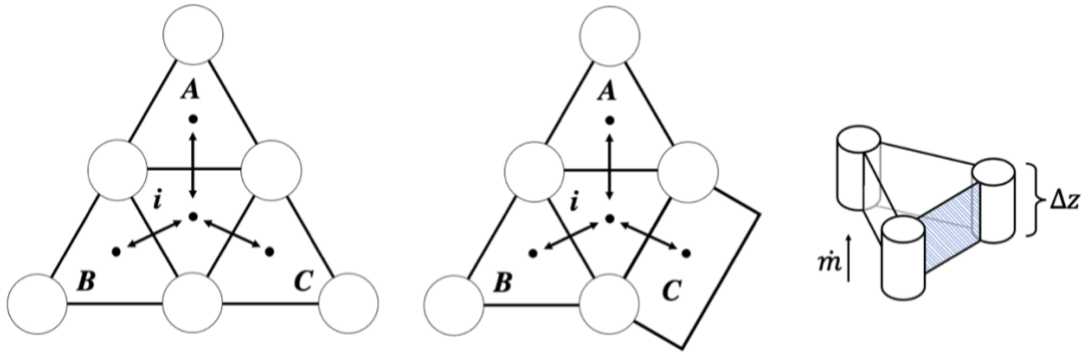


Figure 8. Subchannel adjacency illustrations for interior-type subchannels.

To obtain the net heat flux at the centroid of subchannel  $i$ , the heat fluxes at the cell interfaces are substituted using a finite difference formulation. Equation 3-11 shows this step for the connection between subchannel  $i$  and subchannel  $A$ . The distance between the centroids of subchannel  $i$  and subchannel  $A$  is denoted as  $L_{Ai}$ .

$$A_{A,i} \left. \frac{\partial T}{\partial r} \right|_{A,i} = A_{A,i} \frac{T_A - T_i}{L_{Ai}}. \quad (3-11)$$

The result of this treatment is that the radial heat flux terms reduce to 1-D conduction, producing the equation described as the energy-balance method in most of the existing SUPERENERGY literature. Equation 3-12 shows the energy balance equation for interior subchannels obtained by applying the preceding steps to Equation 3-9. In Equation 3-12, conduction to adjacent subchannels has been collected into a summation over the adjacent subchannels that exchange heat across the faces  $f$  of subchannel  $i$ .

$$\rho C_p v_{i,z} V_i \frac{\partial T_i}{\partial z} = q_i + k^* \sum_f A_{fi} \frac{T_f - T_i}{L_{fi}}. \quad (3-12)$$

With radial heat transfer resolved, heat transfer in the axial direction (on the LHS of Equation 3-12) can now be discretized. As defined in Equation 3-7,  $v_{i,z}$  is the axial velocity in subchannel  $i$ , which is equal to the ratio of subchannel axial volumetric flow rate and cross-sectional flow area in the x-y plane,  $A_{i,xy}$ . Given that, the product of  $\rho$  and  $v_{i,z}$  is  $m_{i,z}/A_{i,xy}$ , where  $m_{i,z}$  is the coolant axial mass flow rate in subchannel  $i$ . Then,  $V_i/A_{i,xy} = \Delta z$ . These steps on the LHS of Equation 3-12 are shown in Equation 3-13.

$$\rho C_p v_{i,z} V_i \frac{\partial T_i}{\partial z} = \frac{m_{i,z}}{A_{i,xy}} C_p V_i \frac{\partial T}{\partial z} = m_{i,z} C_p \Delta z \frac{\partial T}{\partial z} \quad (3-13)$$

The derivative with respect to  $z$  is expanded into the difference between two axial planes,  $j$  and  $j + 1$ . This results in the cancellation of  $\Delta z$  on the LHS. The terms on the RHS of Equation 3-12 are evaluated at axial plane  $j$ . The result is the relationship shown in Equation

**3-14.** By assuming that all interior subchannels have the same mass flow rate,  $m_{1,z}$  – the mass flow rate in any interior subchannel – has been substituted into Equation **3-14**. This is an explicit formulation, which is the same as that implemented in SUPERENERGY-2.

$$m_{1,z}C_p(T_{i,j+1} - T_{i,j}) = q_{i,j} + k^* \sum_f A_{fi} \frac{T_{f,j} - T_{i,j}}{L_{fi}}. \quad (3-14)$$

$m_{1,z}$  = axial mass flow rate (kg/s) in an interior subchannel

Equation **3-14** is used to obtain coolant temperatures at the  $j + 1$  axial plane based on the temperatures at the  $j$  axial plane for all interior (Type 1) subchannels. As shown in Figure 8, interior subchannels can have interfaces with (1) three interior subchannels or (2) two interior subchannels and one edge subchannel. Incorporating the distances between subchannel centroids for these two configurations produces Equations **3-15** and **3-16**, respectively. The  $\Delta z$  on the RHS comes from the expansion of  $A_{fi}$  based on assembly dimensions.

$$T_{i,j+1} = T_{i,j} + \frac{q_{i,j}}{m_{1,z}C_p} + \frac{(\rho C_p \varepsilon + \kappa k)d_{pp}\Delta z}{m_{1,z}C_p} \left( \frac{T_{A,j} + T_{B,j} + T_{C,j} - 3T_{i,j}}{L_{11}} \right). \quad (3-15)$$

$$T_{i,j+1} = T_{i,j} + \frac{q_{i,j}}{m_{1,z}C_p} + \frac{(\rho C_p \varepsilon + \kappa k)d_{pp}\Delta z}{m_{1,z}C_p} \left( \frac{T_{A,j} + T_{B,j} - 2T_{i,j}}{L_{11}} + \frac{T_{C,j} - T_{i,j}}{L_{12}} \right). \quad (3-16)$$

where:  $L_{11}$  = distance between interior subchannel centroids (m)  
 $L_{12}$  = distance between interior-edge subchannel centroids (m)

### 3.4 Region II: Edge and corner subchannels

The heat transfer in edge and corner subchannels is more complex than that in interior subchannels due to (a) the need to incorporate the circumferential (swirl) flow, and (b) the heat transfer between the coolant and the duct wall. Application of the assumptions introduced in

Subsection 3.2 to Equation **3-3** in Region II results in Equation **3-17** for heat transfer in an edge or corner type subchannel  $i$ .

$$\rho C_p v_{i,z} \frac{\partial T_i}{\partial z} = q_i''' + q_s''' + q_w''' + k^* \nabla_{xy} \cdot \nabla_{xy} T_i. \quad (3-17)$$

where:  $v_{i,z}$  = axial velocity (m/s) in subchannel  $i$   
 $q_s'''$  = heat addition (W/m<sup>3</sup>) to subchannel  $i$  due to swirl flow  
 $q_w'''$  = heat addition (W/m<sup>3</sup>) to subchannel  $i$  from convection with duct

The LHS in Equation **3-17** represents axial convection in subchannel  $i$ . The terms on the RHS represent heat addition to subchannel  $i$  due to heating from pins, convective swirl flow from a neighboring subchannel, convection from the duct wall, or conduction with adjacent subchannels. Once again, the conduction term on the RHS is limited to the x-y-plane. Taking the volume integral over Equation **3-17** and using the same divergence theorem substitution as applied for Region I on the conduction term yields Equation **3-18**.

$$\rho C_p v_{i,z} V_i \frac{\partial T_i}{\partial z} = q_i + q_s + q_w + k^* \int_S \nabla_{xy} T_i \cdot n dS \quad (3-18)$$

Using the same rationale as for Region I, the heat flux surface integral in the conduction term on the RHS of Equation **3-18** can be expanded over the adjacent subchannel mesh cells. The heat transferred from the duct wall is included as a new term,  $q_w$ .

$$C_p v_{i,z} V_i \frac{\partial T_i}{\partial z} = q_i + q_s + q_w + k^* \sum_f A_{fi} \frac{T_f - T_i}{L_{fi}}. \quad (3-19)$$

As was done for Region I, the derivative on the LHS of Equation **3-19** can be split into a finite difference relationship to apply axial discretization. Axial convection takes place between axial planes  $j$  and  $j + 1$  for subchannel  $i$ . As was done for the interior subchannels, the mass flow rate in the axial direction can be introduced into Equation **3-20** by combining the axial velocity, density, and subchannel mesh cell volume.

$$m_{i,z}C_p(T_{i,j+1} - T_{i,j}) = q_{i,j} + q_{s,j} + q_{w,j} + k^* \sum_f A_{fi} \frac{T_{f,j} - T_{i,j}}{L_{fi}}. \quad (3-20)$$

The heat addition from swirl flow and the duct wall can now be expanded. Both are convective heat transfer mechanisms that can be expressed in terms of a heat transfer coefficient. For convective swirl flow, the heat transfer coefficient (W/m<sup>2</sup>K) is equal to the product of the coolant density, heat capacity, and swirl velocity, which is obtained from correlation. The heat transfer area is the product of the axial step size and the gap between the outermost pins and duct wall. The neighbor from which subchannel  $i$  receives heat due to swirl convection depends on the direction of the wire wrap (clockwise or counterclockwise). The swirl velocity term can be expanded in terms of a difference relationship with the appropriate neighboring subchannel, indexed as  $s$ . This is shown in Equation 3-21.

$$q_s = h_s A_{si} (T_{s,j} - T_{i,j}) = \rho C_p v_s d_{pw} \Delta z (T_{s,j} - T_{i,j}) \quad (3-21)$$

where:  $v_s$  = swirl velocity (m/s)  
 $d_{pw}$  = distance between pin and duct wall (m)  
 $T_{s,j}$  = temperature of neighbor from which swirl flow occurs (K)

The heat addition due to convection with the duct wall is shown in Equation 3-22 . The heat transfer coefficient between the coolant and duct wall  $h_{wi}$  (W/m<sup>2</sup>K) is calculated based on a correlated value of the subchannel Nusselt number.

$$q_w = h_{wi} A_{wi} (T_{w,j} - T_{i,j}) \quad (3-22)$$

where:  $h_{wi}$  = subchannel  $i$  coolant-to-duct heat transfer coefficient (W/m<sup>2</sup>K)  
 $A_{wi}$  = heat transfer area (m<sup>2</sup>) with subchannel  $i$  duct wall;  
 If corner:  $A_{wi} = c_{w-out,1} \Delta z$  (where  $c_{w-in,1}$  is the corner half-perimeter of the innermost duct).

The heat transfer area  $A_{wi}$  depends on whether subchannel  $i$  is an edge or corner subchannel. For an edge subchannel, the area is  $L_{22} \Delta z$ , where  $L_{22}$  is the pin pitch. For a corner channel, the area is  $2c_{w-out,1} \Delta z$ , where  $c_{w-out,1}$  is the half-perimeter of the corner subchannel taken at the duct outer surface.

Figure 9 shows the adjacencies for the subchannel mesh cells along the duct wall. In the summation for the conductive heat transfer from adjacent subchannels,  $f = A, B, C$  for a regular edge subchannel mesh, where  $A$  and  $B$  are adjacent edge or corner subchannels, while  $C$  is the adjacent interior subchannel. For corner subchannels,  $f = A, B$  because corner channels connect only to the two adjacent edge (or corner) subchannels. For both duct and corner subchannels, the swirl velocity comes from adjacent edge or corner subchannel  $A$  or  $B$ , depending on the direction of the wire wrap.

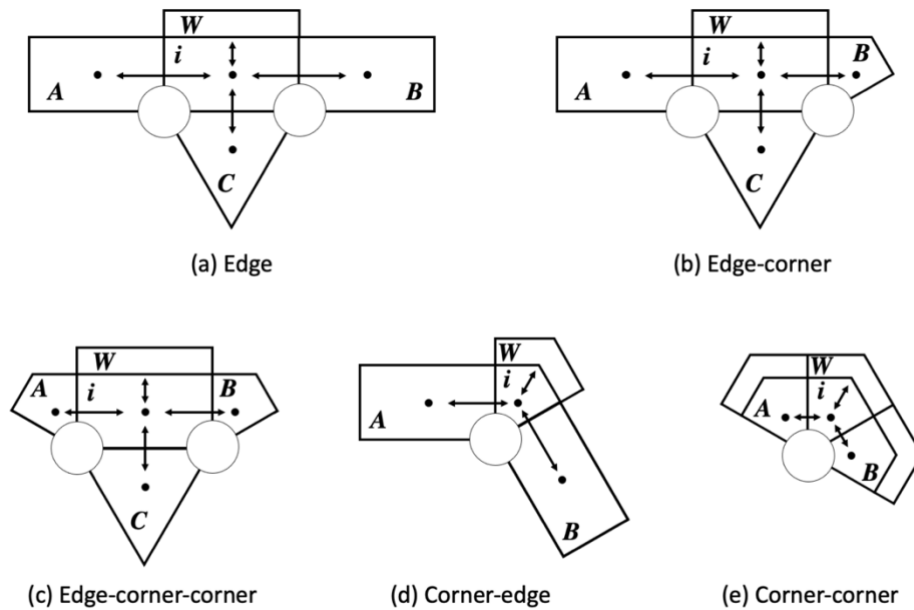


**Figure 9. Adjacencies for subchannels along the duct wall.**

Equations 3-23 through 3-27 describe the energy balance in: an edge subchannel connected to two edge subchannels (3-23); an edge subchannel connected to one edge and one corner subchannel (3-24); an edge subchannel connected to two corner subchannels (3-25); a corner subchannel connected to two edge subchannels (3-26); and a corner subchannel connected to two corner subchannels (3-27). In Equations 3-23 through 3-27,  $m_{2,z}$  is the axial mass flow rate in edge subchannels and  $m_{3,z}$  is the axial mass flow rate in corner subchannels and the swirl flow is assumed to be in a clockwise direction.



$$\begin{aligned}
 T_{i,j+1} = T_{i,j} &+ \frac{q_{i,j}}{m_{2,z}C_p} + \frac{h_{wi}L_{22}\Delta Z}{m_{2,z}C_p}(T_{w,j} - T_{i,j}) \\
 &+ \frac{(\rho C_p \varepsilon + \kappa k)\Delta Z}{m_{2,z}C_p} \left[ d_{pw} \left( \frac{T_{A,j} + T_{B,j} - 2T_{i,j}}{L_{22}} \right) + d_{pp} \left( \frac{T_{c,j} - T_{i,j}}{L_{12}} \right) \right] \\
 &+ \frac{\rho v_s d_{pw}\Delta Z}{m_{2,z}}(T_{A,j} - T_{i,j}).
 \end{aligned} \tag{3-23}$$

$$\begin{aligned}
 T_{i,j+1} = T_{i,j} &+ \frac{q_{i,j}}{m_{2,z}C_p} + \frac{h_{wi}L_{22}\Delta Z}{m_{2,z}C_p}(T_{w,j} - T_{i,j}) \\
 &+ \frac{(\rho C_p \varepsilon + \kappa k)\Delta Z}{m_{2,z}C_p} \left[ d_{pw} \left( \frac{T_{A,j} - T_{i,j}}{L_{22}} + \frac{T_{B,j} - T_{i,j}}{L_{23}} \right) + d_{pp} \left( \frac{T_{c,j} - T_{i,j}}{L_{12}} \right) \right] \\
 &+ \frac{\rho v_s d_{pw}\Delta Z}{m_{2,z}}(T_{A,j} - T_{i,j}).
 \end{aligned} \tag{3-24}$$

$$\begin{aligned}
 T_{i,j+1} = T_{i,j} &+ \frac{q_{i,j}}{m_{2,z}C_p} + \frac{h_{wi}L_{22}\Delta Z}{m_{i,z}C_p}(T_{w,j} - T_{i,j}) \\
 &+ \frac{(\rho C_p \varepsilon + \kappa k)\Delta Z}{m_{2,z}C_p} \left[ d_{pw} \left( \frac{T_{A,j} + T_{B,j} - 2T_{i,j}}{L_{23}} \right) + d_{pp} \left( \frac{T_{c,j} - T_{i,j}}{L_{12}} \right) \right] \\
 &+ \frac{\rho v_s d_{pw}\Delta Z}{m_{2,z}}(T_{A,j} - T_{i,j}).
 \end{aligned} \tag{3-25}$$

$$\begin{aligned}
 T_{i,j+1} = T_{i,j} &+ \frac{q_{i,j}}{m_{3,z}C_p} + \frac{2h_{wi}c_{w-out,1}\Delta Z}{m_{3,z}C_p}(T_{w,j} - T_{i,j}) \\
 &+ \frac{(\rho C_p \varepsilon + \kappa k)d_{pw}\Delta Z}{m_{3,z}C_p} \left( \frac{T_{A,j} + T_{B,j} - 2T_{i,j}}{L_{23}} \right) + \frac{\rho v_s d_{pw}\Delta Z}{m_{3,z}}(T_{A,j} - T_{i,j})
 \end{aligned} \tag{3-26}$$

$$\begin{aligned}
 T_{i,j+1} = T_{i,j} &+ \frac{q_{i,j}}{m_{3,z}C_p} + \frac{2h_{wi}c_{w-out,1}\Delta Z}{m_{3,z}C_p}(T_{w,j} - T_{i,j}) \\
 &+ \frac{(\rho C_p \varepsilon + \kappa k)d_{pw}\Delta Z}{m_{3,z}C_p} \left( \frac{T_{A,j} + T_{B,j} - 2T_{i,j}}{L_{33}} \right) + \frac{\rho v_s d_{pw}\Delta Z}{m_{3,z}}(T_{A,j} - T_{i,j})
 \end{aligned} \tag{3-27}$$

### 3.5 Flowing bypass and inter-assembly gap coolant

This subsection describes the heat transfer through the coolant in the bypass gap of double-ducted assemblies and the gap between adjacent assemblies. There are two types of bypass gap subchannels: side subchannels (Type 6) and corner subchannels (Type 7). Because each type of bypass gap subchannel is in contact with two other coolant subchannels and two duct walls, the adjacency definition for both subchannel types is the same.

For brevity, the derivation starts from the energy balance for the gap subchannels, shown in Equation 3-28. In the bypass gap between ducts there are no pins to distort heat flow, so the shape factor  $\kappa$  on the thermal conductivity is omitted. Because there are no wire-wrapped pins, eddy diffusivity and swirl velocity are neglected. In DASSH, it is assumed that no neutron or gamma heating takes place in the bypass gap coolant. Convection boundaries (Equation 3-22) are applied at the interfaces between the coolant and the duct walls. The heat transfer coefficient for both duct walls is assumed to be the same, as they rely on the same coolant properties and velocity. For both types of bypass gap subchannels, the indices  $d$  and  $f$  in Equation 3-28 correspond to the two adjacent duct walls and coolant subchannels, respectively.

$$m_{i,z} C_p (T_{i,j+1} - T_{i,j}) = \sum_d q_{w,d} + k \sum_f A_{fi} \frac{T_{f,j} - T_{i,j}}{L_{fi}}. \quad (3-28)$$

The axial mass flow rate in each bypass subchannel is calculated as a fraction of the total bypass flow rate based on subchannel area.  $m_{6,z}$  denotes the mass flow rate in edge subchannels while  $m_{7,z}$  denotes the mass flow rate in the corner subchannels of the bypass gap.

Equations 3-29 through 3-33 describe heat transfer in bypass gap subchannels: edge subchannels connected to two other edge subchannels (3-29); side subchannels connected to one side and one corner subchannel (3-30); side subchannels connected to two corner subchannels (3-31); corner subchannels connected to two edge subchannels (3-32); and corner subchannels connected to two corner subchannels (3-33).

$$T_{i,j+1} = T_{i,j} + \frac{h_{wi}L_{22}\Delta z}{m_{6,z}C_p}(T_{w1,j} + T_{w2,j} - 2T_{i,j}) + \frac{k\Delta z d_{byp}}{m_{6,z}C_p} \left( \frac{T_{C,j} + T_{D,j} - 2T_{i,j}}{L_{22}} \right) \quad (3-29)$$

$$\begin{aligned} T_{i,j+1} = T_{i,j} + \frac{h_{wi}L_{22}\Delta z}{m_{6,z}C_p}(T_{w1,j} + T_{w2,j} - 2T_{i,j}) \\ + \frac{k\Delta z d_{byp}}{m_{6,z}C_p} \left( \frac{T_{C,j} - T_{i,j}}{L_{22}} + \frac{T_{D,j} - T_{i,j}}{L_{67}} \right) \end{aligned} \quad (3-30)$$

$$T_{i,j+1} = T_{i,j} + \frac{h_{wi}L_{22}\Delta z}{m_{6,z}C_p}(T_{w1,j} + T_{w2,j} - 2T_{i,j}) + \frac{k\Delta z d_{byp}}{m_{6,z}C_p} \left( \frac{T_{C,j} + T_{D,j} - 2T_{i,j}}{L_{67}} \right) \quad (3-31)$$

$$\begin{aligned} T_{i,j+1} = T_{i,j} + \frac{2h_{wi}\Delta z}{m_{7,z}C_p} [c_{w-out,1}(T_{w1,j} - T_{i,j}) + c_{w-out,2}(T_{w2,j} - T_{i,j})] \\ + \frac{k\Delta z d_{byp}}{m_{7,z}C_p} \left( \frac{T_{C,j} + T_{D,j} - 2T_{i,j}}{L_{67}} \right) \end{aligned} \quad (3-32)$$

$$\begin{aligned} T_{i,j+1} = T_{i,j} + \frac{2h_{wi}\Delta z}{m_{7,z}C_p} [c_{w-out,1}(T_{w1,j} - T_{i,j}) + c_{w-out,2}(T_{w2,j} - T_{i,j})] \\ + \frac{k\Delta z d_{byp}}{m_{7,z}C_p} \left( \frac{T_{C,j} + T_{D,j} - 2T_{i,j}}{L_{77}} \right) \end{aligned} \quad (3-33)$$

The formulation for inter-assembly heat flow is like bypass duct flow in that there are no wire-wrapped pins present to influence the flow regime. Like for the bypass gap, it is assumed that there is no heat generation in the inter-assembly gap coolant. Therefore, Equation 3-28 applies to the inter-assembly gap as well. For the gap subchannel, the indices  $d$  and  $f$  in Equation 3-28 correspond to the two adjacent duct walls and coolant subchannels, respectively; for the gap-corner subchannel,  $d$  and  $f$  correspond to the three adjacent duct walls and coolant subchannels, respectively.

Figure 10 shows the adjacency definitions of the two types of inter-assembly gap subchannels. Coolant in the gap-side subchannel interfaces with two duct walls and has two connections to the coolant in adjacent gap subchannels, which may both be gap-side subchannels, one gap-side and one-gap corner, or two gap-corners. Coolant in the gap-corner

subchannel interfaces with three duct walls and has connections to the coolant in three adjacent subchannels, which may be gap-side or gap corner subchannels.

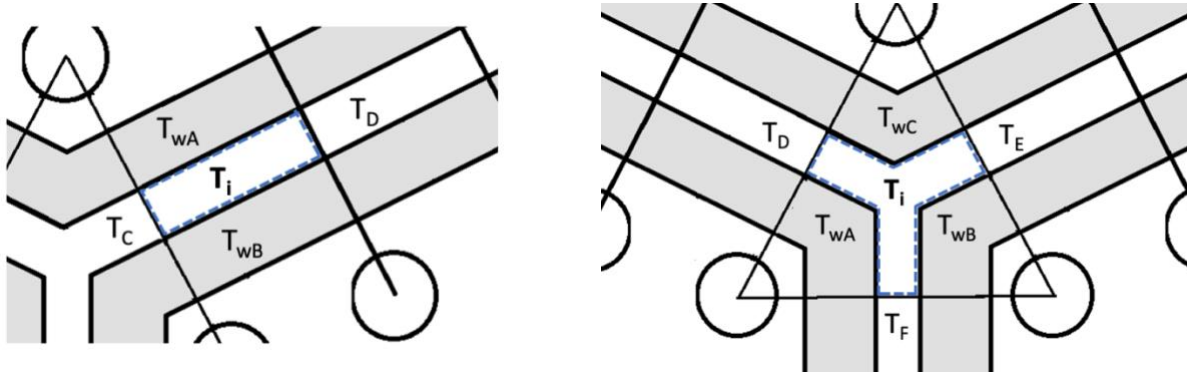


**Figure 10. Inter-assembly gap and gap-corner subchannels in single-ducted assemblies**

In Figure 10, the three adjacent assemblies shown all have the same pin lattice such that the subchannel meshing in the inter-assembly gap is in perfect agreement. In DASSH, the gap is meshed to match with the adjacent assembly with the most pins, thereby creating the finest possible gap meshing. Disagreement will arise when two adjacent assemblies have different pin lattices. When that occurs, an energy conserving restriction and projection operation are used to meld the coarse and fine mesh results, the details of which are discussed in Section 3.7. For the solution of the inter-assembly gap, the subchannel representation used for the equations to follow always have the finest mesh representation.

The dimensions for the inter-assembly gap subchannels are given in Figure 1 and Figure 3. DASSH assumes that the width of the inter-assembly gap is constant throughout the core; in other words, the outer hexagonal dimension of all assemblies must be equal. However, because the size of each gap subchannel depends on pin bundle geometry of the assemblies adjacent to it, subchannel dimensions and parameters can vary throughout the core. Although the gap width is constant, other variable parameters include: subchannel area, distance between subchannels, interface surface area with adjacent duct walls, mass flow rate, and heat transfer coefficient.

For brevity, Equation 3-34 shows a general form of the inter-assembly gap subchannel energy balance that covers all possible adjacency types for both gap-edge and gap-corner subchannels. In Equation 3-34, the second term accounts for heat transfer from the adjacent

duct walls. Gap-edge subchannels are adjacent to at most two duct walls whereas gap-corner subchannels are adjacent to at most three duct walls. The heat transfer coefficient and mass flow rate are specific to the subchannel. The surface area between the duct and subchannel is dependent on the specific subchannel-wall connection, to accommodate the nonsymmetrical shape of corner-gap subchannels between dissimilar assemblies. Gap subchannels at the outer domain boundary exchange heat only with the assemblies to which they are adjacent; omitting heat transfer with the surface that marks the domain boundary establishes an adiabatic condition. The third term in Equation 3-34 represents conduction between adjacent gap subchannels. The summation is over all adjacent subchannels  $f$ , and the parameter  $L_{fi}$  is the distance between them and subchannel  $i$ . Gap-edge subchannels always connect to two other subchannels, but gap-corner subchannels may connect to either two or three other subchannels.

$$T_{i,j+1} = T_{i,j} + \frac{h_i \Delta z}{m_{i,z} C_p} \sum_{w=1}^W P_{w,i} (T_{w,j} - T_{i,j}) + \frac{k \Delta z d_{\text{gap}}}{m_{i,z} C_p} \sum_{f=1}^F \frac{T_{f,j} - T_{i,j}}{L_{fi}}. \quad (3-34)$$

where:  $P_{w,i}$  = wetted perimeter (m) of interface between wall  $w$  and subchannel  $i$   
 $d_{\text{gap}}$  = gap width (m)

In Equation 3-34, the coolant temperatures at the  $j + 1$  axial plane have been determined based on the coolant and duct temperatures in the  $j$  axial plane. Once the coolant temperatures have been obtained for at any axial plane, the duct temperatures at that level may be determined.

### 3.6 Stagnant inter-assembly gap coolant models

For plant efficiency, the coolant flow rate in the inter-assembly gap is generally minimal. Under this circumstance, the flow in the inter-assembly gap can be driven by natural convection, where gravity forces are important. With low coolant mass flow rate and nearly stagnant inter-assembly gap coolant, the axial mesh size required to ensure stability can be extremely small. This problem was first observed in SUPERENERGY-2, which offered a second model for inter-assembly gap coolant that neglected axial heat transfer in the gap and assumed the coolant was a simple conductive material. The error introduced by neglecting axial heat transfer in the inter-

assembly was expected to be small [2]. DASSH offers two models that approximate the inter-assembly gap as a stagnant coolant.

### 3.6.1 Model 1: Conduction model

In the conduction model, heat is transferred via conduction from the duct wall surface to the center of the inter-assembly gap. The inter-assembly gap coolant film temperature is assumed equal to the duct wall surface temperature. Heat can be transferred via conduction between adjacent gap coolant subchannels. With no axial heat transfer, the energy balance collapses to that shown in Equation 3-35.

$$0 = q_{convection} + q_{conduction} \quad (3-35)$$

The first term in Equation 3-35 is a summation over all conduction connections with adjacent duct walls  $w$ . The second term is a summation over all conduction connections with adjacent gap coolant subchannels  $f$ . Expanding these two terms gives the following expression, where the summations in the first and terms are over the adjacent duct wall surfaces and adjacent coolant subchannels, respectively.

$$0 = \frac{k\Delta z}{d_{gap}/2} \sum_{w=1}^W P_{w,i}(T_w - T_i) + k\Delta z d_{gap} \sum_{f=1}^F \frac{(T_f - T_i)}{L_{fi}} \quad (3-36)$$

The RHS of equation 3-36 can be viewed as modified forms of Terms 2 and 3 in Equation 3-34. The interface areas between subchannel  $i$  and adjacent subchannels and duct walls are dependent on  $\Delta z$ . The equation can be rearranged to calculate  $T_i$ , which is assigned as the subchannel temperature at axial plane  $j + 1$  and is calculated based on adjacent coolant and duct wall temperatures at axial plane  $j$ . The resulting equations resemble a weighted average of the adjacent wall and coolant temperatures. The conduction model formulation is shown in a general form in Equation 3-37. The numerator contains the convection and conduction components of heat transfer with adjacent walls and subchannels, respectively.

$$T_{i,j+1} = \frac{\left[ \frac{2}{d_{gap}} \sum_{w=1}^W P_{w,i} T_{w,j} + d_{gap} \sum_{f=1}^F \frac{T_{f,j}}{L_{fi}} \right]}{\frac{2}{d_{gap}} \sum_{w=1}^W P_{w,i} + d_{gap} \sum_{f=1}^F \frac{1}{L_{fi}}} \quad (3-37)$$

### 3.6.2 Model 2: Duct-average model

In the duct-average model, the inter-assembly gap coolant temperature equals the average of the adjacent duct wall temperatures (in Equation 3-38,  $W$  is the number of adjacent duct walls). Because conduction between adjacent gap subchannels will likely have only a small effect on coolant temperatures, it is expected that this model closely approximates the conduction model (Model 1) with less computational expense.

$$T_{i,j+1} = \frac{1}{W} \sum_{w=1}^W T_{w,j} \quad (3-38)$$

### 3.6.1 Energy balance error

Because it will not be transferred out of the system via axial convection, stagnant inter-assembly gap coolant should not accumulate energy at steady state. In DASSH, a full domain solver is avoided by introducing the lagged duct wall boundary condition. The introduction of a conductive medium instead of a convective medium in both stagnant gap models introduces an inconsistency in the boundary conditions for the lagged information, causing an energy imbalance. The magnitude of the energy balance error is reported in the regular output. It is a function of how much energy is transferrable between assemblies and thus the relative temperature difference between assemblies at any given axial height and the effective conductivity of the gap coolant. Observed errors are less than 1% for the fast reactor problems studied thus far.

Future work will reformulate these gap models to eliminate the intermediate step and create a direct thermal connection between the coolant subchannels in adjacent assemblies, as is done in SUPERENERGY-2.

### 3.7 Treating mesh disagreement in the inter-assembly gap

Solving the coolant temperatures in the subchannels that comprise the inter-assembly gap, as shown in the preceding subsection, requires the duct wall temperatures of the adjacent assemblies. If the adjacent assemblies have different pin bundle geometries, the meshing of the interface will disagree as shown in Figure 11. This subsection describes how DASSH accommodates these disagreements.

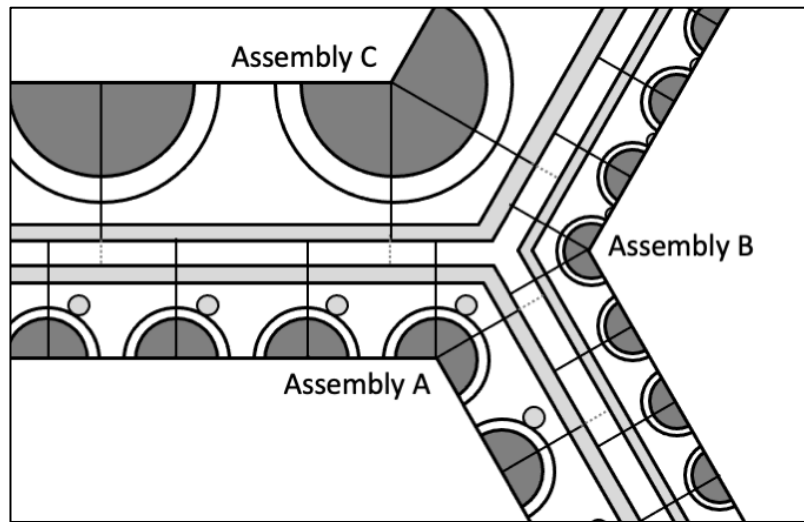


**Figure 11. Example of possible disagreement in subchannel meshing between adjacent assemblies**

When subchannel mesh disagreements arise, the inter-assembly gap is discretized based on the adjacent assembly with the finer mesh. Duct wall surface temperatures are known for each assembly at axial level  $j$ . For assemblies with coarser mesh than the adjacent inter-assembly gap, the coarse-mesh duct temperatures are projected by distributing heat to the fine inter-assembly gap mesh. Then, with all duct wall surface temperatures known on the inter-assembly gap mesh, all inter-assembly gap subchannel temperatures at the  $j + 1$  axial level are solved. To calculate duct temperatures at the  $j + 1$  axial level, heat from the fine inter-assembly gap mesh must be restricted back to the duct coarse mesh.

#### 3.7.1 Projection of coarse wall temperatures to fine inter-assembly gap mesh

The projection of heat from the coarse duct mesh to the fine inter-assembly mesh is diagrammed in Figure 12 for a simple system in which a portion of two coarse mesh wall



elements are adjacent to one inter-assembly gap coolant element. The energy balance requires that the total energy removed from wall elements must be equal to the energy received by any adjacent inter-assembly gap element.

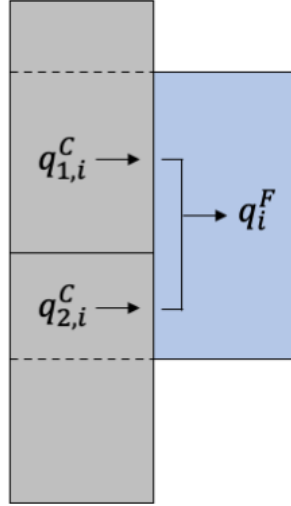


**Figure 12. Mesh disagreement between inter-assembly gap subchannel and two duct elements**

In Figure 12,  $q_{1,i}^C$  and  $q_{2,i}^C$  are the heat transferred from the first and second adjacent wall elements to the active gap element, respectively;  $q_i^F$  is the energy transferred to/from the gap element from the adjacent wall elements. This is generalized in Equation 3-39.

$$q_i^F = \sum_{w=1}^W q_{w,i}^C \quad (3-39)$$

where:  $q_i^F$  = heat (W) transferred into/out of fine mesh subchannel  $i$   
 $q_{w,i}^C$  = heat (W) transferred between subchannel  $i$  and adjacent wall elements  $w$

In Equation 3-39,  $W$  is the number of wall elements that interface with gap subchannel  $i$ . Each of the terms in the summation on the RHS of Equation 3-39 can be expanded based on the equation for convective heat transfer, resulting in Equation 3-40.

$$q_i^F = \sum_{w=1}^W h_{w,i} A_{w,i} (T_w - T_i) \quad (3-40)$$

where:  $h_{w,i}$  = heat transfer coefficient (W/m<sup>2</sup>K) between subchannel  $i$  and wall  $w$   
 $A_{w,i}$  = interface area (m<sup>2</sup>) between subchannel  $i$  and wall  $w$   
 $T_w$  = temperature (K) of wall  $w$   
 $T_i$  = temperature (K) of subchannel  $i$

Because the heat transfer coefficient into a particular inter-assembly gap element is defined based on the parameters of that element, it is the same for all adjacent wall elements and is removed from the summation, as shown in Equation 3-41.

$$q_i^F = h_i \sum_{w=1}^W A_{w,i} (T_w - T_i) \quad (3-41)$$

The expression inside of the summation can be expanded and separated into two summation terms, as shown in Equation 3-42.

$$q_i^F = h_i \sum_{w=1}^W A_{w,i} T_w + h_i \sum_{w=1}^W A_{w,i} T_i \quad (3-42)$$

In the second term of Equation 3-42, the temperature is not dependent on the summation index and can be moved from the inside of that term. Then, the summation of the interface areas  $A_{w,i}$  is equal to the total interface area of gap element  $i$ , denoted  $A_i$ . These simplifications result in Equation 3-43.

$$q_i^F = h_i \sum_{w=1}^W A_{w,i} T_w + h_i A_i T_i \quad (3-43)$$

$A_i$  = total interface area (m<sup>2</sup>) between subchannel  $i$  and the duct wall

DASSH calculates heat transfer between the wall and gap using a wall temperature as the boundary condition. An average wall boundary condition can be obtained based on Equation 3-44, which implies that the average wall temperature is equal to a weighted average of adjacent wall temperatures based on interface area.

$$T_w^* = \frac{1}{A_i} \sum_{w=1}^W A_{w,i} T_w \quad (3-44)$$

Substituting Equation 3-44 into Equation 3-43 results in the convection boundary condition expression used in the inter-assembly gap coolant temperature calculation, with  $T_w^*$  used as the average adjacent wall temperature on the inter-assembly gap fine mesh.

$$q_i^F = h_i A_i (T_w^* - T_i) \quad (3-45)$$

To obtain  $T_w^*$  for every inter-assembly gap fine mesh element, Equation 3-45 is solved for each assembly in the core using matrix operations. The duct surface temperatures for each assembly are arranged in a vector,  $\vec{T}_w$  with length  $N_{wall}$ . To project from the  $N_{wall}$  wall elements to the  $N_{gap}$  adjacent inter-assembly elements, the matrix  $\mathbf{P} \in \mathbb{R}^{N_{gap} \times N_{wall}}$  is constructed based on the overlap between wall and gap meshes. It is used in the matrix operation shown in Equation 3-46. The result is the vector  $\vec{T}_w^*$ , which has length  $N_{gap}$ .

$$\vec{T}_w^* = \mathbf{P} \vec{T}_w \quad (3-46)$$

### 3.7.2 Restriction of fine inter-assembly gap temperatures to coarse wall mesh

The restriction of fine-mesh inter-assembly gap temperatures to be used in the coarse duct wall calculation is carried out using a similar procedure as for the projection described in the previous section. Figure 13 shows the interface between some fine-mesh inter-assembly gap elements and a single wall element. The energy balance requires that all heat transferred away from the gap coolant must be gained by the adjacent duct wall. This balance is generalized in Equation 3-47.

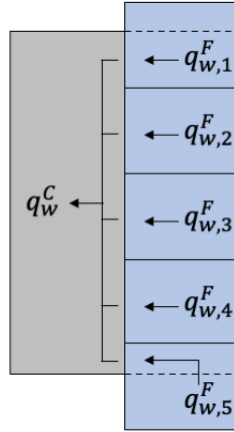


**Figure 13. Mesh disagreement between duct element and inter-assembly gap subchannels**

$$q_w^C = \sum_{i=1}^I q_{w,i}^F \quad (3-47)$$

where:  $q_w^C$  = heat (W) transferred into/out of coarse duct element  $w$   
 $q_{w,i}^F$  = heat (W) transferred between duct element  $w$  and fine-mesh inter-assembly gap subchannels  $i$

The summation in Equation 3-47 is over all  $I$  inter-assembly gap subchannels adjacent to duct wall element  $w$ . Substituting the convection heat transfer expression into the summation in Equation 3-47 results in Equation 3-48.

$$q_w^C = \sum_{i=1}^I h_{w,i} A_{w,i} (T_w - T_i) \quad (3-48)$$

where:  $h_{w,i}$  = heat transfer coefficient (W/m<sup>2</sup>K) between subchannel  $i$  and wall  $w$   
 $A_{w,i}$  = interface area (m<sup>2</sup>) between subchannel  $i$  and wall  $w$   
 $T_w$  = temperature (K) of wall  $w$   
 $T_i$  = temperature (K) of subchannel  $i$

The expression inside of the summation can be expanded and separated into two summation terms, as shown in Equation 3-49.

$$q_w^C = \sum_{i=1}^I h_{w,i} A_{w,i} T_w + \sum_{i=1}^I h_{w,i} A_{w,i} T_i \quad (3-49)$$

The wall temperature calculation (see Subsection 3.8) requires a temperature boundary condition. As for the projection operation, the restriction requires the definition of an average temperature. Because the heat transfer coefficient can vary between inter-assembly gap subchannels, the average must be weighted by the heat transfer coefficient as well as the interface area. An expression for average temperature is shown in Equation 3-50. Additionally, an expression for the average heat transfer coefficient, defined as a weighted average of the heat transfer coefficients in the adjacent gap subchannels based on interface area, is shown in Equation 3-51. These averages were defined to conserve energy based on the boundary conditions applied in the 1-D conduction model described in Section 3.8.

$$T_i^* = \frac{1}{A_w h_i^*} \sum_{i=1}^I h_{w,i} A_{w,i} T_i \quad (3-50)$$

$$h_i^* = \frac{1}{A_w} \sum_{i=1}^I A_{w,i} h_{w,i} \quad (3-51)$$

To obtain the convection heat transfer expression based on Equations 3-50 and 3-51, they can be substituted into the second and first terms in Equation 3-49, respectively. The result is shown in Equation 3-52.

$$q_i^C = h_i^* A_w (T_w - T_i^*) \quad (3-52)$$

Like for the projection operation, the restriction operation is carried out by matrix operation based on interface area between the wall and inter-assembly gap meshes.

The adjacent inter-assembly gap coolant temperatures for each assembly are arranged in a vector,  $\vec{T}_i$  with length  $N_{gap}$ . To project from the  $N_{gap}$  adjacent inter-assembly gap subchannels to the  $N_{wall}$  adjacent wall elements, the matrix  $\mathbf{R} \in \mathbb{R}^{N_{wall} \times N_{gap}}$  is constructed

based on the overlap between wall and gap meshes. It is used in matrix operations, as shown in Equations 3-53 and 3-54. The result is the vector  $\vec{T}_i^*$ , which has length  $N_{wall}$ . Note that the vector multiplication and matrix division shown in 3-54 are element-wise operations.

$$\vec{h}_i^* = R\vec{h}_i \quad (3-53)$$

$$\vec{T}_i^* = \frac{R(\vec{h}_i\vec{T}_i)}{R\vec{h}_i} \quad (3-54)$$

### 3.8 Duct walls

The coolant temperatures in the  $j + 1$  axial plane are determined based on the coolant and duct wall temperatures in the  $j$  axial region. Heat should be transferred between the coolant and duct wall at the same axial plane as the entire domain is fully coupled. However, this over-constrains the duct temperatures because there are coolant channels on both sides of the duct walls requiring a substantially more complex formulation than that shown here. In SE2-ANL and DASSH, this complexity is avoided by allowing the duct wall temperatures to lag axially behind the coolant temperatures. Once the coolant temperatures at the  $j + 1$  axial plane are known, the duct wall temperatures at the  $j + 1$  axial plane can be determined. These are then used in the calculation of the coolant temperatures at axial plane  $j + 2$ . It is expected that the error between using a fully coupled system and the one chosen should be minimized by choosing a sufficiently small axial mesh size.

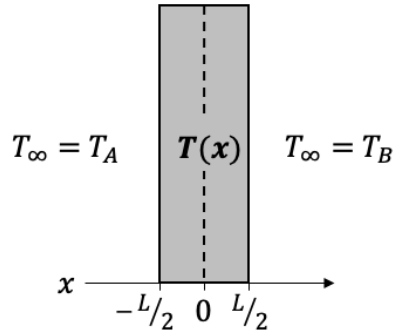


**Figure 14. Diagram of duct wall 1-D heat transfer model**

Ducts in both single- and double-ducted assemblies have coolant on both sides and can be described by the 1-D system shown in Figure 14. Axial conduction through the duct and conduction between adjacent duct cells is assumed to be negligible. Heat is generated inside the duct by neutron and gamma heating. The equation describing this system is:

$$\frac{d^2T}{dx^2} + \frac{q'''}{k} = 0. \quad (3-55)$$

By integrating twice, the solution to Equation 3-56 is obtained:

$$T(x) = \frac{-q'''}{2k}x^2 + c_1x + c_2 \quad (3-56)$$

Note that for the units in Equation 3-56 to agree,  $c_1$  must have units of temperature per length, while  $c_2$  must have units of temperature. Convection boundary conditions are applied between the adjacent coolant channels and the duct walls, as shown in Equations 3-57 and 3-58. The duct wall temperatures are not yet known but are not required for determination of the integration constants.

$$-k \frac{dT}{dx} \Big|_{x=-L/2} = h_A \left( T_A - T \left( x = -\frac{L}{2} \right) \right) \quad (3-57)$$

$$k \frac{dT}{dx} \Big|_{x=L/2} = h_B \left( T_B - T \left( x = \frac{L}{2} \right) \right) \quad (3-58)$$

Evaluating Equation 3-56 and its derivative at the boundaries enables the determination of  $c_1$  (units of K/m) and  $c_2$  (units of K) as:

$$c_1 = \frac{\frac{q'''L}{2} \left( \frac{h_A}{h_B} - 1 \right) + h_A(T_B - T_A)}{h_AL + k \left( 1 + \frac{h_A}{h_B} \right)} \quad (3-59)$$

$$c_2 = T_B + q''' \left( \frac{L^2}{8k} + \frac{L}{2h_B} \right) - c_1 \left( \frac{L}{2} + \frac{k}{h_B} \right) \quad (3-60)$$

With that Equations 3-56, 3-59, and 3-60, the duct centerline temperature (at  $x = 0$ ) and wall surface temperatures (at  $x = \pm L/2$ ) can be solved.

The corner duct wall elements create a slight inconsistency because they are not one dimensional: the inner surface area is less than the outer surface area. To rectify this, it is assumed that all duct heat transfer across corner ducts occurs through the outer surface area. This means, for example, that heat transfer via convection in the corner subchannel in the pin bundle takes place over the outer corner surface area rather than the inner surface area. This choice was made so that energy would be conserved when using that same heat transfer area on the outer surface of the duct. The impact on the temperature distribution is negligible.

### 3.9 Numerical stability and axial-mesh size requirements

Because DASSH utilizes a forward-differencing scheme to march axially through the core, numerical stability of the solution can be guaranteed by using a very fine axial mesh. This section presents the axial mesh size requirement for each type of coolant subchannel. The mesh size must be sufficiently fine to prevent the occurrence of any negative temperatures in the system. The mesh size constraint,  $\Delta z$ , is defined with an extreme energy-loss case for each subchannel, in which the subchannel coolant receives no internal heat generation and the adjacent temperatures are equal to zero. After carrying out a step in this system, the temperature of subchannel coolant must be greater than or equal to zero. An axial mesh size constraint is



determined for all types of subchannels in every assembly; the global minimum requirement is imposed across the entire system.

The derivation of the constraint will be illustrated in detail for an interior subchannel connected to three other interior subchannels. The remaining constraints are listed thereafter. For that interior subchannel, described by Equation 3-15, the extreme energy-loss case described above results in the inequality shown in Equation 3-61, in which  $T_{i,j+1}$  has been set to zero.

$$0 \leq T_{i,j} + \frac{(\rho C_p \varepsilon + \kappa k) d_{pp} \Delta z}{m_{1,z} C_p} \left( \frac{-3T_{i,j}}{L_{11}} \right). \quad (3-61)$$

Dividing both sides by  $T_{i,j}$  and rearranging Equation 3-61 yields the following inequality requirement for  $\Delta z$ :

$$\Delta z \leq \frac{m_{1,z} C_p L_{11}}{3(\rho C_p \varepsilon + \kappa k) d_{pp}}. \quad (3-62)$$

Although Equation 3-62 applies only to one type of coolant subchannel, it highlights how different parameters affect axial stability. In particular, subchannels with low mass flow rate will require smaller axial mesh sizes – this is especially important for the inter-assembly gap, where in SUPERENERGY-2 it was well understood that sufficient flow was required to have a tractable problem. The axial mesh size requirements for the remaining subchannels are described below; the bullets contain references to the equations that present the energy balance for this type of subchannel.

- Interior subchannel connected to two interior subchannels and one edge subchannel (see Equation 3-16)

$$\Delta z \leq \frac{m_{1,z} C_p}{\left( \frac{2}{L_{11}} + \frac{1}{L_{12}} \right) (\rho C_p \varepsilon + \kappa k) d_{pp}}, \quad (3-63)$$

- Edge subchannel connected to an interior subchannel and two edge subchannels (see Equation 3-23)

$$\Delta z \leq \frac{1}{\frac{h_{wi}L_{22}}{m_{2,z}C_p} + \frac{(\rho C_p \varepsilon + \kappa k)}{m_{2,z}C_p} \left( \frac{d_{pp}}{L_{21}} + \frac{2d_{pw}}{L_{22}} \right) + \frac{\rho v_s d_{pw}}{m_{2,z}}}, \quad (3-64)$$

- Edge subchannel connected to interior, edge, and corner subchannels (see Equation 3-24)

$$\Delta z \leq \frac{1}{\frac{h_{wi}L_{22}}{m_{2,z}C_p} + \frac{(\rho C_p \varepsilon + \kappa k)}{m_{2,z}C_p} \left( \frac{d_{pp}}{L_{21}} + \frac{d_{pw}}{L_{22}} + \frac{d_{pw}}{L_{23}} \right) + \frac{\rho v_s d_{pw}}{m_{2,z}}}, \quad (3-65)$$

- Edge subchannel connected to an interior subchannel and two corner subchannels (see Equation 3-25)

$$\Delta z \leq \frac{1}{\frac{h_{wi}L_{22}}{m_{2,z}C_p} + \frac{(\rho C_p \varepsilon + \kappa k)}{m_{2,z}C_p} \left( \frac{d_{pp}}{L_{21}} + \frac{2d_{pw}}{L_{23}} \right) + \frac{\rho v_s d_{pw}}{m_{2,z}}}, \quad (3-66)$$

- Corner subchannel connected to two edge subchannels (see Equation 3-26)

$$\Delta z \leq \frac{1}{\frac{h_{wi}C_{w-out,1}}{m_{3,z}C_p} + \frac{2(\rho C_p \varepsilon + \kappa k)d_{pw}}{m_{3,z}C_p L_{23}} + \frac{\rho v_s d_{pw}}{m_{3,z}}}, \quad (3-67)$$

- Corner subchannel connected to two corner subchannels (see Equation 3-27)

$$\Delta z \leq \frac{1}{\frac{h_{wi}C_{w-out,1}}{m_{3,z}C_p} + \frac{2(\rho C_p \varepsilon + \kappa k)d_{pw}}{m_{3,z}C_p L_{33}} + \frac{\rho v_s d_{pw}}{m_{3,z}}}, \quad (3-68)$$

- Double-duct bypass edge subchannel connected to two edge subchannels (see Equation 3-29)

$$\Delta z \leq \frac{1}{\frac{2h_{wi}L_{22}}{m_{6,z}C_p} + \frac{2kd_{byp}}{m_{6,z}C_pL_{22}}}, \quad (3-69)$$

- Double-duct bypass edge subchannel connected to edge and corner subchannels (see Equation 3-30)

$$\Delta z \leq \frac{1}{\frac{2h_{wi}L_{22}}{m_{6,z}C_p} + \frac{kd_{byp}}{m_{6,z}C_p} \left( \frac{1}{L_{22}} + \frac{1}{L_{67}} \right)}, \quad (3-70)$$

- Double-duct bypass edge subchannel connected to two corner subchannels (see Equation 3-31)

$$\Delta z \leq \frac{1}{\frac{2h_{wi}L_{22}}{m_{6,z}C_p} + \frac{2kd_{byp}}{m_{6,z}C_pL_{67}}}, \quad (3-71)$$

- Double-duct bypass corner subchannel connected to two edge subchannels (see Equation 3-32)

$$\Delta z \leq \frac{1}{\frac{2h_{wi}[c_{w-out,1} + c_{w-out,2}]}{m_{7,z}C_p} + \frac{2kd_{byp}}{m_{7,z}C_pL_{67}}}, \quad (3-72)$$

- Double-duct bypass corner subchannel connected to two corner subchannels (see Equation 3-33)

$$\Delta z \leq \frac{1}{\frac{2h_{wi}[c_{w-out,1} + c_{w-out,2}]}{m_{7,z}C_p} + \frac{2kd_{byp}}{m_{7,z}C_pL_{77}}}, \quad (3-73)$$

- Inter-assembly gap subchannels are evaluated individually because the mesh is not constant throughout the core. Equation 3-74 shows a general form of the constraint for any inter-assembly gap mesh based on Equation 3-34. The convection and conduction

contributions to the constraint are summations over all adjacent duct walls and all connections to adjacent subchannels, respectively.

$$\Delta z \leq \frac{1}{\frac{h_i}{m_{i,z} C_p} \sum_{w=1}^W P_{w,i} + \frac{k d_{gap}}{m_{i,z} C_p} \sum_{a=1}^A \frac{1}{L_{ai}}}, \quad (3-74)$$

### 3.10 Applicability of solution method

The forward-marching solution methodology utilized in DASSH is applicable only in the forced convection flow regime. In assemblies with large pin power skew and low flow rate, the coolant on the side of the assembly with higher heat generation will rise more rapidly than the coolant on the opposite side of the assembly. This buoyancy effect skews the velocity profile. When this occurs, free convection contributes significantly to coolant flow and the forced convection assumption does not apply [11].

SUPERENERGY-2 offered a predictive indicator for whether the forced convection assumption would be broken by the power distribution and assigned flow rate in each assembly. That indicator – based on a modified Grashof number,  $Gr^*$  – was derived in Ref. [11] and reported succinctly in Ref. [2]. The modified Grashof number is defined as follows:

$$Gr^* = \frac{Gr}{f Re^2} \chi \quad (3-75)$$

where:  $f$  = friction factor, based on correlation  
 $Re$  = Reynolds number based on interior subchannel axial velocity and hydraulic diameter; evaluated at assembly mean temperature

In Equation 3-75,  $Gr$  is the Grashof number, defined in Equation 3-76 below:

$$Gr = \frac{g_0 \beta (T_{out} - T_{in}) D_{e1}^3}{\nu^2}. \quad (3-76)$$

where:  $g_0$  = acceleration due to gravity ( $m/s^2$ )  
 $\beta$  = volumetric expansion coefficient at bundle mean temperature  
 $T_M$  = estimated average coolant outlet temperature, based on power, flow rate, and average heat capacity (K)  
 $T_{in}$  = coolant inlet temperature (K)

$D_{e1}$  = hydraulic diameter of interior subchannel  
 $\nu$  = kinematic viscosity at bundle mean temperature ( $\text{m}^2/\text{s}$ )

The volumetric expansion coefficient is evaluated based on values of coolant density taken at two temperatures near the bundle mean temperature. The multiplier  $\chi$  in Equation 3-75 modifies the Grashof number based on power skew:

$$\chi = \frac{\hat{Q}_p - 1}{2M \Gamma L} \quad (3-77)$$

where:  $\hat{Q}_p$  = peak-to-average radial pin power skew  
 $M$  = Novendstern friction factor constant (see Section 4).  
 $L$  = assembly length

and

$$\Gamma = \frac{16 \left( \frac{P}{D} - 1 \right)}{\pi d_{FTF}} \left[ X_1 \epsilon_{1L}^* + \frac{\kappa}{\text{RePr}} \right]. \quad (3-78)$$

where:  $P$  = pin pitch (m)  
 $D$  = pin outer diameter (m)  
 $d_{FTF}$  = duct inner flat-to-flat distance (m)  
 $X_1$  = interior subchannel flow split  
 $\epsilon_{1L}^*$  = dimensionless eddy diffusivity  
 $\kappa$  = conduction shape factor  
 $\text{Pr}$  = coolant Prandtl number at mean temperature

When  $\text{Gr}^* \geq 0.02$ , buoyancy effects become important. This condition is met for most assemblies with sufficiently large coolant mass flow rates (roughly,  $m \geq 0.5 \text{ kg/s}$ ). The criterion is evaluated for each assembly at the beginning of the solution procedure. The solution procedure continues even if the criterion is violated. The outcome is reported in a table in the summary output. If the volumetric expansion coefficient or power skew are zero, the criteria are not reported but the calculation is allowed to proceed.

### 3.11 Pressure drop

The pressure drop along the assembly axial dimension is determined using the Darcy-Weisbach equation (Equation 3-79) with a friction factor obtained from correlation. The correlations for friction factor are discussed in Section 4. In the pin bundle, the equation can be

generalized to any subchannel  $i$  by using subchannel-specific values for friction factor, hydraulic diameter, and velocity.

$$\Delta p = f \frac{\rho v^2 L}{2 D_e} \quad (3-79)$$

where:  $f$  = friction factor  
 $v$  = average velocity (m/s) in the rod bundle  
 $L$  = length (m) of the rod bundle  
 $D_e$  = equivalent hydraulic diameter (m)

In general, DASSH calculates pressure drop in the pin bundle similarly to SUPERENERGY-2. One difference between DASSH and SUPERENERGY-2 is that in SUPERENERGY-2 the correlations for friction factor are evaluated once at the beginning of the calculation with material properties taken at the average of the core inlet and outlet temperatures, but DASSH updates the friction factor at each axial level to account for changes in material properties with variable temperature. The incremental pressure drop is evaluated for each axial mesh throughout the axial sweep. As temperature increases, density decreases, resulting in an increase in velocity and Re and a decrease in the friction factor. Evaluated on an ABR-1000 fuel assembly, the cumulative impact on the total pressure drop in the pin bundle – for an assembly for which the core-average temperature is representative – is less than  $\pm 1\%$  compared to the result using material properties and friction factor evaluated at the core-average temperature.

### **3.12 Low-fidelity models**

In SUPERENERGY-2, pins were assumed to extend throughout the entire length of the assembly. However, upper and lower reflectors are common in fast reactor assemblies and they have almost always have a different geometry than the pin bundle. Treating these regions with the pin bundle model is inaccurate and causes unnecessary computational expense. The main aspects of heat transfer to/from these regions can be captured by a simpler model.

To that end, DASSH offers the user the option of utilizing a low-fidelity model in lieu of the pin bundle model. With the low-fidelity model, DASSH aims to capture the key physical

phenomena – heat generation and inter-assembly heat transfer – while minimizing computational expense. The low-fidelity model can be applied to axial regions above and/or below the pin bundle to an entire assembly. This subsection first introduces the DASSH low-fidelity model and the parameters it relies on. Then, the specific usage of low-fidelity models to approximate pin-bundle regions is discussed. Finally, the method by which DASSH connects axial regions is covered.

### 3.12.1 Model description

The low-fidelity model treats the interior of the assembly as a homogeneous mixture of coolant and structural materials, discretized as shown in Figure 15. The coolant volume fraction is based on user input. One coolant temperature is calculated for the assembly at each axial step. Axial heat transfer occurs via forced convection. Radial heat transfer occurs by convection with the duct wall through six duct meshes centered at the corners. Heat generation occurs directly in the coolant.

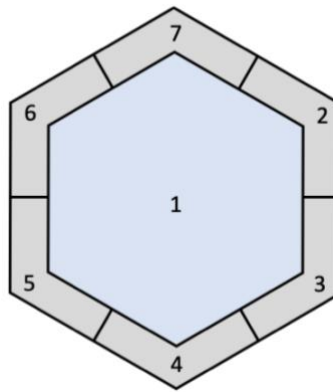


**Figure 15. Coolant and duct subchannels for the low-fidelity assembly model**

The energy balance formulation for the coolant based on the heat transfer mechanisms discussed above is shown in Equation 3-80. It resembles the energy balance applied to edge and corner subchannels in the pin bundle model, with some small differences. In Equation 3-80, the second term on the RHS is heat generation in the coolant. The third term is convection with the duct walls.

$$T_{j+1} = T_j + \frac{q}{m_z C_p} + \frac{h_w P_d \Delta z}{m_z C_p} \left( \sum_{f=1}^6 T_{w,f,j} - T_j \right). \quad (3-80)$$

where:  $m_z$  = axial mass flow rate (kg/s) in assembly  
 $P_d$  = duct wall inner perimeter

The low-fidelity model still requires an axial constraint, albeit one that is significantly less limiting than that of an equivalent pin bundle model. The axial constraint, derived in the same way as those in the previous section, is shown in Equation 3-81.

$$\Delta z \leq \frac{m_z C_p}{h_w P_d} \quad (3-81)$$

Pressure drop in the low-fidelity model system is calculated using the Darcy-Weisbach formula with friction factors evaluated based on user-input and flow regime. The user can input parameters that characterize the geometry of the region: namely, the hydraulic diameter and the surface roughness (epsilon). If not specified, the hydraulic diameter is calculated using an estimated wetted perimeter obtained by treating the non-coolant volume as a cylinder. The friction factor is calculated as shown below, where the equation for the turbulent friction factor is a hybrid of multiple correlations based on the Colebrook equation as presented in Equation 15 in [12]. The transition regime friction factor is a linear interpolation between the laminar and turbulent values, as shown in Equation 3.3-206 in [13].

If  $Re < 2200$ :

$$f_L(Re) = \frac{64}{Re} \quad (3-82)$$

if  $Re > 3000$ :

$$f_T(Re) = \left[ -2 \log_{10} \left( \frac{\frac{\epsilon}{D_e}}{3.7} - \frac{4.518}{Re} \log_{10} \left( \frac{6.9}{Re} + \left[ \frac{\frac{\epsilon}{D_e}}{3.7} \right]^{1.11} \right) \right) \right]^{-2} \quad (3-83)$$



Otherwise:

$$f_{Tr}(Re) = f_L(2200) + \left[ 3.75 - \frac{8250.0}{Re} \right] (f_T(3000) - f_L(2200)) \quad (3-84)$$

where:  $f_L$  = friction factor for laminar flow regime  
 $f_T$  = friction factor for turbulent flow regime  
 $f_{Tr}$  = friction factor for transition flow regime  
 $\varepsilon$  = surface roughness

### 3.12.2 Approximating pin bundles with low-fidelity model

In cases where an assembly has a very low flow rate and generates low power, such as outer shield assemblies, it may be advantageous to model the pin bundle with a low-fidelity model to relax the axial constraint. DASSH provides an option for users to input pin-bundle parameters to the low-fidelity model. In that case, coolant volume fraction is calculated based on pin-bundle geometry. DASSH determines the appropriate correlated friction factor and calculate pressure drop as if the region were a pin bundle.

It is critical to note that with only one coolant channel, the low-fidelity model does not capture heat transfer through the coolant in the same way as the pin-bundle model, which discretizes the coolant radially. In the low-fidelity model, heat generated in the assembly is immediately available for heat transfer with the duct wall, whereas in the pin-bundle model, heat added to subchannels that are not adjacent to the duct walls is not available for convective heat transfer. When pin-bundle parameters are used as input to the low-fidelity model, DASSH compensates for this by calculating the heat transfer coefficient  $h_w$  using an effective thermal conductivity based on the minimum lateral porosity. This accounts for the fact that conduction through the coolant from the center of the assembly to the edge is impeded by the pins. In the case of a pin-bundle geometry, heat must be conducted around the pins. This effect is well-captured by accounting for the bundle the minimum lateral porosity,  $\lambda = 1 - (D/P)$ , which is plotted in Figure 16 as a function of bundle pitch-to-diameter ratio [9].

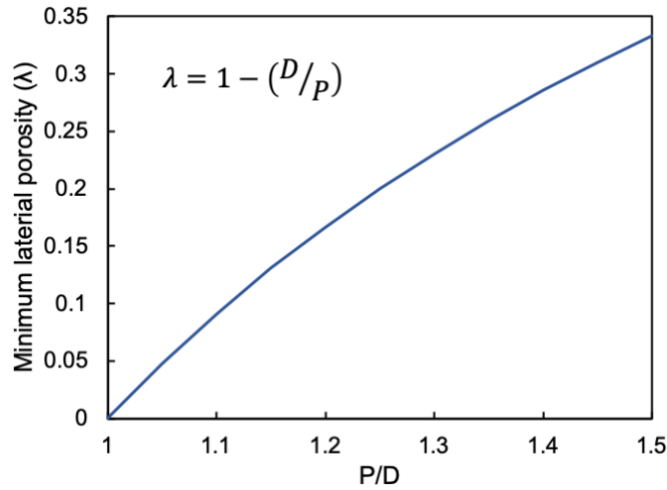


**Figure 16. Minimum lateral porosity as a function of pin bundle pitch-to-diameter ratio.**

The resulting effective thermal conductivity used for calculating the heat transfer coefficient is shown below in Equation 3-85. DASSH will calculate the lateral porosity ( $\lambda$ ), conductivity shape factor ( $s^*$ ), and eddy diffusivity ( $\varepsilon$ ) parameters based on the input pin-bundle parameters. The combination of bulk conductivity enhancement due to turbulent mixing and reduction due to lateral porosity captures the major behaviors of radial heat transfer in the pin bundle model.

$$k_{porous} = \lambda(k s^* + \rho C_p \varepsilon) \quad (3-85)$$

where:  $\lambda$  = minimum lateral porosity

### 3.12.3 Combination of axial regions in an assembly

In DASSH, low-fidelity models can be applied to non-bundle regions above and below the pin bundle. If desired by the user, multiple different low-fidelity models can be applied above and below the pin bundle to represent different axial regions in the assembly. Figure 17 shows a schematic of an assembly with four low-fidelity axial regions, two above and two below the pin bundle.

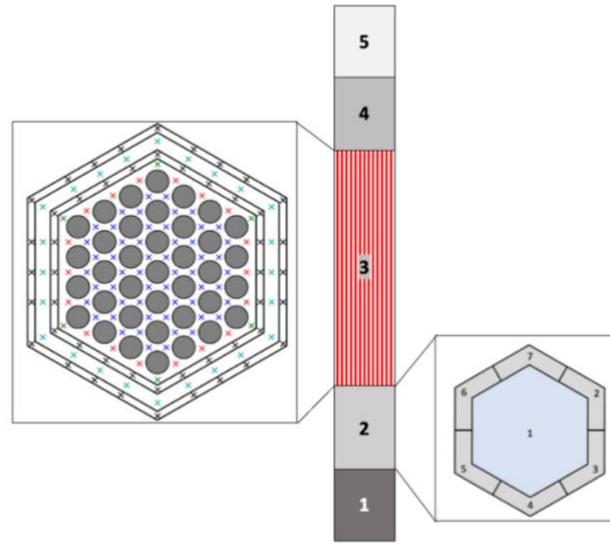


**Figure 17. Diagram showing example combination of axial regions in an assembly**

When changing between axial regions, a projection or restriction operation is required. To transition from a low-fidelity to pin-bundle model at axial level  $j$ , the coolant temperature in every higher fidelity subchannel is set equal to the average coolant temperature. If the pin bundle in the new region has multiple ducts, the temperatures of all bypass channels are set to the average coolant temperature. All ducts except the outermost duct are set equal to the average temperature. When transitioning from a pin-bundle region to a low-fidelity model region, the single coolant temperature is set equal to the average coolant temperature from the pin-bundle region, including all bypass channels.

Once the coolant temperatures have been averaged in the new region, the temperature of the outermost duct is calculated at axial level  $j$  with the duct meshing in the new region, based on the coolant temperatures in the new region. This repeat of the duct wall calculation is necessary to ensure that energy is balanced when utilizing duct temperatures in the calculation for the next axial step.

### **3.13 Convection approximation**

As described in the previous subsections, DASSH handles convection with the duct wall using a correlated heat transfer coefficient and the temperature of the subchannel coolant and

the duct wall surface. For coolant materials such as liquid metal, the Nusselt number does not approach 0 even as the mass flow rate approaches zero. The result is that low flow rates can result in strict axial mesh size requirements due to the convection term because of high values for the heat transfer coefficient.

To mitigate this effect, DASSH can model convection with the duct wall in the same way as was done in SUPERENERGY-2, which was to use a lumped resistance that included the heat transfer coefficient and conduction through the wall to the duct mid-wall. The extra component to the thermal resistance improves the axial mesh size requirement by about an order of magnitude and produces nearly the same numerical result (generally to within 0.5%). Equation 3-86 and Equation 3-87 compare the default and approximated convective terms.

$$\frac{h_w A_i}{m_{i,z} C_p} (T_{w,j} - T_{i,j}) \quad (3-86)$$

$$\left[ \frac{x}{2k_w} + \frac{1}{h_w} \right]^{-1} \frac{A_i}{m_{i,z} C_p} (T_{mw,j} - T_{i,j}) \quad (3-87)$$

where:  $A_i$  = area of interface between subchannel and duct wall  
 $x$  = duct wall thickness (m)  
 $k_w$  = duct wall thermal conductivity (W/m-K)  
 $T_{mw,j}$  = duct mid-wall temperature (K)

This “convection approximation” can be enabled or disabled by the user and is engaged by DASSH for assemblies that have axial mesh size requirements smaller than the user-provided minimum value.

### 3.14 Energy balance calculation

DASSH calculates two energy balances throughout the solution procedure: one on the coolant inside each assembly, and one on the inter-assembly gap coolant. Heat is added to the coolant within assemblies by heating and is transferred radially away from the assemblies, into and out of the inter-assembly gap, by convection with duct walls.

For coolant in the assembly interior (within the innermost duct), energy is added directly to the coolant from heat generation in the pins. With every step of the calculation, for each assembly, the total energy given to the coolant from heat generation is added to a running tally. Additionally, the edge and corner subchannels exchange heat with the duct wall via convection. At every step of the calculation, the energy exchanged with the duct walls is added to a running tally for each edge and corner subchannel, based on the following equation.

$$Q_{conv} = h_w A (T_w - T_i) \quad (3-88)$$

where:  $h_w$  = coolant-to-wall heat transfer coefficient (W/m<sup>2</sup>K)  
 $A$  = area of interface between subchannel and duct wall (m<sup>2</sup>)

For assemblies with multiple duct walls and bypass gaps between them, the coolant in the bypass gap exchanges heat via conduction with both duct walls. These are also treated with Equation 3-88. When heat transfer between assemblies is disabled, the assembly will not transfer any heat through the outermost duct wall.

These energy tallies are maintained separately for each axial region that comprises an assembly. When the calculation is complete, the tallies for each region are combined and energy balance on the assembly can be assessed with Equation 3-89, which equates the energy added from heat generation in the pins and/or coolant, the total energy added/lost through the duct wall, and the energy that produced the resulting coolant temperature rise. Heat generation in the duct wall is included in  $Q_{conv}$ .

$$Q_{in} + Q_{conv} - Q_{\Delta T} = 0.0 \quad (3-89)$$

where:  $Q_{in}$  = energy added to coolant from heat generation (W)  
 $Q_{conv}$  = energy added/removed through convection with duct wall (W)  
 $Q_{\Delta T}$  = energy to achieve resulting coolant temperature rise (W)

In Equation 3-89, the energy from coolant temperature rise  $Q_{\Delta T}$  is calculated based on the mass flow rate and outlet temperature in each subchannel, as shown below:

$$Q_{\Delta T} = C_p \sum_{i=1}^{N_{sc}} m_i \Delta T_i \quad (3-90)$$

where:  $C_p$  = heat capacity at assembly axial-average temperature (J/kg-K)  
 $m_i$  = mass flow rate in subchannel  $i$  (kg/s)  
 $\Delta T_i$  = temperature rise in subchannel  $i$  (K)

The energy balance shown in Equation 3-89 holds to within numerical precision if static coolant material properties are used. If coolant properties are allowed to vary, the use of the average heat capacity in Equation 3-90 will result in a small error in the final energy balance.

Equation 3-88 is also used to track the energy balance on the inter-assembly gap subchannels, which gain and lose energy only by convection with adjacent duct walls. The contribution of energy to a subchannel from each adjacent duct wall is tracked separately. When the flowing inter-assembly gap model is used, heat is removed from the gap by forced convection and  $Q_{\Delta T}$  for the inter-assembly gap coolant is nonzero. The following equation is used to determine the overall core energy balance.

$$\sum_{a=1}^{N_{asm}} Q_{in,a} - \sum_{a=1}^{N_{asm}} Q_{\Delta T,a} - Q_{\Delta T,gap} = 0.0 \quad (3-91)$$

where:  $Q_{in,a}$  = total power added to pins, duct, and coolant in assembly  $a$  (W)  
 $Q_{\Delta T,a}$  = energy associated with temperature rise in assembly  $a$  or in the inter-assembly gap (W)

Depending on the options employed in the calculation, the core total energy balance may show a small error (generally on the order of 0.1% of the core total power). First, if power is distributed to the duct walls, error is introduced because the duct wall temperatures are lagged a step behind the coolant temperatures. If the duct wall generates heat between steps  $j - 1$  and  $j$ , it cannot transmit that heat to the coolant via convection until the step from  $j$  to  $j + 1$ . By then the coolant temperatures are elevated from accepting heat from adjacent pins and direct heating. Second, use of one of the non-flowing inter-assembly gap heat transfer models results in a small error in the energy balance because heat is accumulated in the inter-assembly gap coolant and not removed from the core. These errors have been observed to be less than 1% of the total core power based on fast reactor models studied thus far.

Because the energy contributions from adjacent assemblies to inter-assembly gap subchannels are tracked separately, DASSH can report heat transferred between assemblies and the inter-assembly duct. The values in the table are calculated at each step for the connections between each coolant subchannel and each adjacent duct wall over the axial sweep, then accumulated per hex face in the DASSH standard output. Because the inter-assembly gap corner subchannels are not necessarily symmetrical, heat is distributed between sides according to the interface area of the corner on each hex face. Heat not transferred between assemblies is removed by the inter-assembly gap coolant when the flowing inter-assembly gap model is used.

### 3.15 Pin temperatures

DASSH calculates pin temperatures by treating the clad, gap, and fuel with a 1-D radial conduction model for concentric cylinders with no axial conduction, applied to each axial plane in the coolant grid. The temperature at each cylindrical shell inner surface is evaluated based on the temperature at the outer surface. By marching through successive shells, the clad and fuel temperatures are obtained.

#### 3.15.1 Coolant temperatures

The other boundary condition is the adjacent coolant temperature, obtained by averaging the temperatures of the coolant subchannels surrounding the pin based on surface area fraction (each interior and corner subchannel contacts 1/6 of the pin surface; for edge subchannels, the fraction is 1/4).

$$T_{cool} = \sum_i x_i T_i \quad (3-92)$$

where:  $T_{cool}$  = average pin-adjacent coolant temperature (K)  
 $i$  = pin-adjacent subchannel index  
 $x_i$  = subchannel-pin surface area fraction  
 $T_i$  = subchannel coolant temperature (K)

#### 3.15.2 Clad temperatures

The clad outer temperature is determined using a heat transfer coefficient based on a correlated value for the Nusselt number.

$$T_{clad,out} = T_{cool} + \frac{q'}{h_c 2\pi R_{pin}} \quad (3-93)$$

where:  $q'$  = pin linear power (W/m)  
 $h_c$  = coolant-to-pin heat transfer coefficient (W/m<sup>2</sup>K)  
 $R_{pin}$  = pin outer radius (m)

All heat is assumed to be generated in the fuel; none is generated in the clad. The effect of this assumption is minor because the fraction of heat generated in the clad is less than 1% of the total pin power. The result of including additional heat in the fuel is a slight overestimation of fuel temperature. Heat transfer in the clad occurs according to the 1-D cylindrical conduction relationship shown below.

$$T_{clad,in} = T_{clad,out} + \frac{q'}{2\pi \bar{k}_{clad}} \ln \left( \frac{R_{pin}}{R_{pin} - d_{clad}} \right) \quad (3-94)$$

where:  $d_{clad}$  = clad thickness (m)  
 $\bar{k}_{clad}$  = clad thermal conductivity (W/m-K); evaluated by iteration  
 $R_{pin}$  = pin outer radius (m)

Equation **3-95** is solved to obtain the clad inner surface temperature. Iterations are required to update the clad thermal conductivity with temperature. An arithmetic average is used to determine the average clad thermal conductivity based on its values at the temperatures of the clad inner and outer surface. The clad outer surface temperature is used as the initial guess for the clad inner surface temperature.

$$\bar{k}_{clad} = \frac{k_{clad}(T_{clad,in}) + k_{clad}(T_{clad,out})}{2} \quad (3-95)$$

Convergence is achieved when successive iterations produce clad inner surface temperatures that are different by less than 0.001 K. Once converged, Equation **3-95** is solved again using the thermal conductivity found via iteration to determine the clad mid-wall temperature.



### 3.15.3 Fuel surface temperature

With the clad inner surface temperature determined, the fuel surface temperature can be calculated based on heat transfer across the fuel-clad gap, if present. The user specifies whether a gap is present and if so, what material occupies it. If there is no gap, the fuel surface temperature is set equal to the clad inner surface temperature. If a gap is present, the temperature at the fuel surface is calculated by iteration with the following equations. Just like for the clad temperature calculation, the thermal conductivity of the gap is updated for each iteration, this time based on the harmonic mean of the temperatures on the clad inner surface and fuel outer surface.

$$T_{f,out} = T_{clad,in} + \frac{q'}{2\pi k_{gap}} \ln \left( \frac{R_{pin} - d_{clad}}{R_f} \right) \quad (3-96)$$

where:  $T_{f,out}$  = fuel outer surface temperature (K)  
 $R_f$  = fuel pellet outer radius (m)  
 $k_{gap}$  = gap thermal conductivity (W/m-K)

### 3.15.4 Fuel temperatures

The fuel may be divided to allow for specification of different properties that affect fuel thermal conductivity. As such, the cylindrical pellet becomes a system of concentric cylindrical shells around a central cylinder (or void space, if annular fuel). Power density (W/m<sup>3</sup>) is assumed to be constant throughout the pellet. Power density is calculated by dividing the linear pin power (input from power distribution) by the pellet cross-sectional area, as shown in Equation 3-97.

$$q'''_{gen} = \frac{q'}{\pi R_{fuel}^2} \quad (3-97)$$

where:  $q'''_{gen}$  = power density (W/m<sup>3</sup>) in the fuel pellet  
 $q'$  = linear pin power (W/m)  
 $R_{fuel}$  = outer radius (m) of fuel pellet

Figure 18 shows a diagram of one cylindrical shell in this system, for use in deriving the equation used in the fuel model. Heat generated in the fuel inside the highlighted shell,  $q_{in}$ , must be transferred through the shell and out of the fuel. Additionally, heat is generated in the

shell with power density  $q'''_{gen}$ . The governing equation for radial heat conduction in the cylindrical shell is shown in Equation 3-98. The formulation assumes the power density in the pellet to be constant radially,

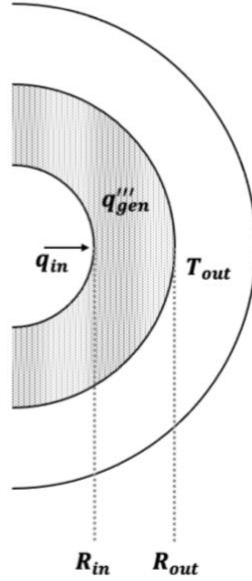


Figure 18. Diagram of fuel pellet shell model system

$$\frac{1}{r} \frac{d}{dr} \left( r \frac{dT}{dr} \right) + \frac{q'''_{gen}}{\bar{k}} = 0 \quad (3-98)$$

where:  $\bar{k}$  = temperature-averaged thermal conductivity (W/m-K)

By integrating Equation 3-98 twice, Equation 3-99 is obtained:

$$T(r) = \frac{-q'''_{gen} r^2}{4\bar{k}} + c_1 \ln(r) + c_2 \quad (3-99)$$

Two boundary conditions are required to evaluate the integration constants: (1) heat flux boundary condition on the inner surface (based on the value of  $q_{in}$ ); (2) temperature boundary

condition on the outer surface. The heat flux boundary condition is evaluated first by Equation **3-100**.

$$-\bar{k} \frac{dT}{dr} \Big|_{r=R_{in}} = \frac{q_{in}}{A_{in}} \quad (3-100)$$

where:  $R_{in}$  = shell inner radius (m)  
 $q_{in}$  = power (W) transferred into active shell from inner shells  
 $A_{in}$  = interface area (m<sup>2</sup>) between active, inner shells ( $= 2\pi R_{in} \Delta z$ )

Solving Equation **3-100** for  $c_1$  yields Equation **3-101**.

$$c_1 = \frac{R_{in}}{\bar{k}} \left[ \frac{q'''_{gen} R_{in}}{2} - \frac{q_{in}}{A_{in}} \right] \quad (3-101)$$

The integration constant  $c_1$  can be simplified by evaluating  $q_{in}$  in terms of the pellet power density,  $q'''_{gen}$ , which is constant throughout the fuel pellet. The relationship between  $q_{in}$  and  $q'''_{gen}$  is shown in Equation **3-102**.

$$q_{in} = q'''_{gen} \pi R_{in}^2 \Delta z \quad (3-102)$$

where:  $\Delta z$  = axial step size (m)

By substituting Equation **3-102** for  $q_{in}$  and expanding  $A_{in}$  as  $2\pi R_{in} \Delta z$ , it is found that  $c_1 = 0$ . The second integration constant,  $c_2$ , is evaluated based on the known temperature at  $R_{out}$ , yielding the expression in Equation **3-103**.

$$c_2 = T_{out} + \frac{q'''_{gen} R_{out}^2}{4\bar{k}} \quad (3-103)$$

where:  $T_{out}$  = temperature (K) on the outer surface of the active shell  
 $R_{out}$  = shell outer radius (m)

The resulting equation for temperature across a radial fuel node is shown in Equation **3-104**, which happens to be the equation for temperature distribution across a cylinder. As such, this equation can also be solved for the fuel centerline temperature at the center of the central cylindrical node by setting  $r = 0$ ).

$$T(r) = \frac{q'''_{gen}(R_{out}^2 - r^2)}{4\bar{k}} + T_{out} \quad (3-104)$$

This equation is used to solve for each fuel node, starting from the known fuel surface temperature. Fuel temperatures are evaluated for each node, marching inward from the fuel surface to the fuel centerline. Once the inner surface temperature of the node is evaluated, it is used as the outer boundary condition for the calculation in the next node. Applying Equation 3-104 to this system results in Equation 3-105.

$$T_{in,i}^{fuel} = \frac{q'''_{gen}(R_{out,i}^2 - R_{in,i}^2)}{4\bar{k}_{fuel,i}} + T_{out,i}^{fuel} \quad (3-105)$$

where:  $T_{in,i}$  = temperature (K) on the inner surface of shell  $i$   
 $R_{out,i}$  = shell  $i$  outer radius (m)  
 $R_{in,i}$  = shell  $i$  inner radius (m)  
 $\bar{k}_i$  = temperature-averaged thermal conductivity (W/m-K) in shell  $i$   
 $T_{out,i}$  = temperature (K) on the outer surface of shell  $i$

Figure 19 illustrates a fuel pellet divided into three radial nodes; this may be abstracted to as many or as few nodes as needed. The figure demonstrates how fuel properties (for example, Pu and Zr fractions and porosity in metal fuels) are defined for each radial node. Because such fuel parameters affect thermal conductivity, the calculation of temperature across a node uses a unique set of user-defined parameters to determine thermal conductivity.

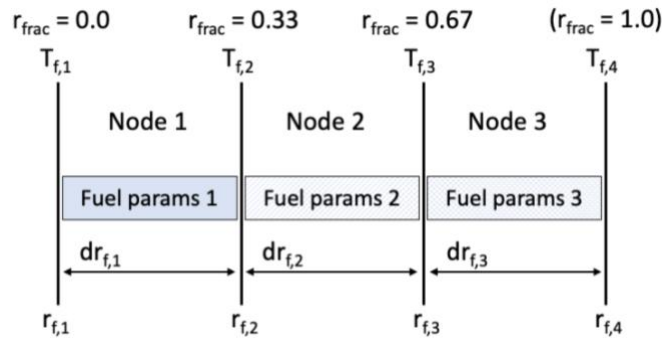


**Figure 19. Diagram illustrating fuel temperature model radial noding**

To solve Equation **3-105**, iterations are required to converge the node inner surface temperature and the temperature-dependent thermal conductivity  $\bar{k}_{fuel,i}$ . The node outer surface temperature is used as the initial guess to calculate thermal conductivity, with which the inner surface temperature can be calculated. The thermal conductivity is calculated with as the arithmetic average of the fuel conductivity evaluated using the inner and outer surface temperatures as shown Equation **3-106**.

$$\bar{k}_{fuel,i} = \frac{k_{fuel,i}(T_{in,i}^{fuel}) + k_{fuel,i}(T_{out,i}^{fuel})}{2} \quad (3-106)$$

Annular fuel may be requested if the user sets the minimum radius to a value greater than zero. In that case, the calculation proceeds until the inner surface of the fuel is reached. The temperature at this point is returned as the pseudo-centerline temperature.

## 4 Review of correlations built into DASSH

Over nearly five decades, researchers have produced numerous correlations characterizing flow in ducted, wire-wrapped, hexagonal-lattice pin bundles. Experimental results have been repeatedly incorporated into new correlations, which are compared against the older correlations for goodness-of-fit to the data. DASSH relies on correlations for friction factors, flow split between subchannels, and mixing parameters to account for transverse flow due to wire wrap. Several correlations are therefore in DASSH to allow the user to assess the impact on their problem.

This section reviews the existing literature to describe these correlations. The studies from which correlations built into DASSH are drawn are those by Novendstern (1972), Rehme (1973), Engle (1979), and Chiu-Rohsenow-Todreas (1980), and Cheng-Todreas (1986). In 2018, the Cheng-Todreas correlations were updated to incorporate new experimental data and correct an update initially proposed in 2013. These studies and the conditions under which they are applicable are summarized in Table 1. Most investigated the friction factor, required to calculate pressure drop, but others studied the flow split and mixing parameters required for the solution methodology employed in DASSH. Taken together, they cover a large range of conditions. In the following subsection, models describing each type of correlation are reported and summarized.

Equations for some of the more complex geometric parameters that characterize pin bundles, such as those for determining subchannel flow areas, wire-wrap area projections, etc., can be found in the cited references. In particular, references [14] and [15] are particularly helpful.

**Table 1. Summary of correlations built into DASSH and their ranges of applicability**

Mixing	Flow split	Bundle friction factor						Bare rod	Ref.
		Investigators	ID	Year	P/D	H/D	Nr	Flow regime (Re)	
Cheng-Todreas	Cheng-Todreas	Novendstern	NOV	1972	1.06 – 1.42	8.0 – 96.0	19 – 217	Transition, turbulent (2600 – 1e5)	No [20]
		Rehme	REH	1973	1.1 – 1.42	8.0 – 50.0	7 – 217	Transition, turbulent (1000 – 3e5)	No [19]
		Engel	ENG	1979	1.067 – 1.082	7.7 – 8.3	19 – 61	Laminar, transition, turbulent (50 – 1e5)	No [18]
		Cheng-Todreas (detailed)	CTD	1986	1.0 – 1.42	4.0 – 52.0	19 – 217	Laminar, transition, turbulent (50 – 1e6)	Yes [14]
		Cheng-Todreas (simple)	CTS	1986	1.025 – 1.42	8.0 – 50.0	19 – 217	Laminar, transition, turbulent (50 – 1e6)	No [14]
		Upgraded Cheng-Todreas (detailed)	UCTD	2018	1.0 – 1.42	8.0 – 52.0	7 – 217	Laminar, transition, turbulent (50 – 1e6)	Yes [17]
Chiu-Rohsenow-Todreas	Chiu-Rohsenow-Todreas	Novendstern	NOV	Same as Novendstern bundle friction factor					
		MIT	MIT	1980	1.063 – 1.28	4.0 – 52.0	7 – 217	Transition, turbulent (4500 – 8.1e4)	No [16]
		CT/UCT	CT/UCT	Same as Cheng-Todreas (detailed or upgraded-detailed) bundle friction factor					
Cheng-Todreas	Cheng-Todreas	MIT	MIT	1978	1.067 – 1.315	4.0 – 52.0	7 – 217	Turbulent (?? – f??)	No [16]
		CT/UCT	CT/UCT	Same as Cheng-Todreas (detailed or upgraded-detailed) bundle friction factor					

#### 4.1 Bundle friction factor

The friction factor is required to calculate the pressure drop along the length of the reactor core. Chun and Seo [21] reviewed the major experiments and models prior to 2001 – Novendstern [20], Rehme [19], Engle [18], and Cheng-Todreas (detailed and simple) [14] – and found that the Cheng-Todreas detailed and simple correlations best fit the experimental data. Since then, there have been two additional reviews of the existing correlations [22] [23]. The Bubelis and Schikorr study [22] recommended avoiding the Cheng-Todreas correlations, which prompted a response from Todreas [23] that identified flaws in their assessment and concluded that the Cheng-Todreas correlations were indeed the most accurate. More recently, upgrade to the CTD correlations were published to improve agreement to newly available data [17]. To determine which friction factor correlation is best for a particular bundle, users are encouraged to review the overarching studies referenced in [21] and [23].

##### 4.1.1 Novendstern (1972)

Novendstern [20] developed a model to predict pressure losses in wire-wrapped pin bundles by determining the flow distribution between the pins theoretically and multiplying the pressure drop for a smooth pipe (obtained using equivalent diameter techniques) by an empirical correction factor that depends on bundle dimensions and flow rate. These correlations were based on previous experimental work by other researchers.

Novendstern defined the effective friction factor as the product of the theoretical friction factor for flow in a smooth pipe, approximated by a modified version of the Colebrook equations, and a multiplication factor used to increase the pressure drop accounting for wire lead and pin pitch-to-diameter ratio.

$$f = M f_s X_1^2 \frac{D_{eb}}{D_{e1}} \quad (4-1)$$

$$f_{smooth} = \left[ 2 \log_{10} \left( -\frac{5.028}{Re_1} \log_{10} \left( \frac{16.76}{Re_1} \right) \right) \right]^2 \quad (4-2)$$



$$M = \left[ \frac{1.034}{\left(\frac{P}{D}\right)^{0.124}} + \frac{29.7 \left(\frac{P}{D}\right)^{6.94} Re_1^{0.086}}{\left(\frac{H}{D}\right)^{2.239}} \right]^{0.885} \quad (4-3)$$

$$Re_1 = \frac{\rho v_1 D_{e1}}{\mu} = Re_b X_1 \frac{D_{e1}}{D_{eb}} \quad (4-4)$$

where:  $Re_i$  = Reynolds no.;  $i$  refers to subchannel type 1 or bundle avg.  
 $D_{ei}$  = hydraulic diam. (m)  
 $X_1$  = flow split parameter for interior subchannel (see Section 4.2).  
 $P$  = pin pitch (m)  
 $D$  = pin diameter (m)  
 $H$  = wire wrap lead length (m)

#### 4.1.2 Rehme (1973)

Rehme [19] determined parameters characterizing pressure drop correlations for hexagonal pin lattices separated by wire wrap using a heated water loop experiment. The primary independent variables in his analysis were: the pitch-to-diameter ratio of the pins (varied by changing the wire diameter while the pin diameter remained the same); the lead of the wire wraps; and the number of pins in the bundle.

$$f = \left( \frac{64}{Re} F^{0.5} + \frac{0.0816}{Re^{0.133}} F^{0.93335} \right) \frac{N_r \pi (D_r + D_w)}{S_t} \quad (4-5)$$

$$F = \left( \frac{P}{D_r} \right)^{0.5} + \left[ 7.6 \frac{(D_r + D_w)}{H} \left( \frac{P}{D_r} \right)^2 \right]^{2.16} \quad (4-6)$$

where:  $Re$  = bundle-average Reynolds number  
 $N_r$  = number of pins in the bundle  
 $D_r$  = diameter (m) of the pins  
 $D_w$  = diameter (m) of the wire wrap  
 $S_t$  = wetted perimeter (m) of the pins and wire wraps  
 $P$  = pin pitch (m)  
 $H$  = wire wrap lead (m)

#### 4.1.3 Engel et al. (1979)

Engel, Markley, and Bishop [18] studied the pressure drop across ducted, wire-wrapped hexagonal 61-pin bundles for different fluids (sodium, water, air) in different flow regimes. They produced correlations for the friction factor in the laminar and turbulent ranges and used these to define the friction factor in the transition range.

$$\begin{array}{ll} \text{Laminar range} & f_L = \frac{110}{Re} \\ Re < 400 & \end{array} \quad (4-7)$$

$$\begin{array}{ll} \text{Turbulent range} & f_T = \frac{0.55}{Re^{0.25}} \\ 5000 < Re < 40000 & \end{array} \quad (4-8)$$

$$\begin{array}{ll} \text{Transition range} & f_{tr} = f_T \left( \frac{Re - 400}{4600} \right)^{0.5} + f_L \left( 1 - \frac{Re - 400}{4600} \right)^{0.5} \\ 400 < Re < 5000 & \end{array} \quad (4-9)$$

#### 4.1.4 Cheng-Todreas Detailed (1986)

Building upon a database of previous and ongoing experimental work, Cheng and Todreas [14] derived friction factors as a function of bundle geometry parameters, contained in a friction factor constant  $C_{fb}$  defined for laminar ( $C_{fL}$ ) and turbulent ( $C_{fT}$ ) flow regimes, and the bundle-average Reynolds number.

$$\begin{array}{ll} \text{Laminar range} & f = \frac{C_{fL}}{Re} \\ Re < Re_{bL} & \end{array} \quad (4-10)$$

$$\begin{array}{ll} \text{Turbulent range} & f = \frac{C_{fT}}{Re^{0.18}} \\ Re > Re_{bT} & \end{array} \quad (4-11)$$

$$\begin{array}{ll} \text{Transition range} & f = \frac{C_{fL}}{Re} (1 - \Psi)^{1/3} + \frac{C_{fT}}{Re^{0.18}} \Psi^{1/3} \\ Re_{bL} < Re < Re_{bT} & \end{array} \quad (4-12)$$

For flow in the transition regime, the friction factor is obtained by a combination of the laminar and turbulent friction factors based on an intermittency factor,  $\Psi$ . The intermittency factor represents the fraction of the flow that is turbulent.

$$\Psi = \frac{\log_{10} Re - \log_{10} Re_{bL}}{\log_{10} Re_{bT} - \log_{10} Re_{bL}} \quad (4-13)$$

where:  $Re$  = bundle-average Reynolds number  
 $Re_{bL}$  = laminar-transition Reynolds number  
 $Re_{bT}$  = transition-turbulent Reynolds number

The intermittency factor relies on Reynolds numbers corresponding to the boundaries between the laminar-transition flow regimes ( $Re_{bL}$ ) and the transition-turbulent flow regimes ( $Re_{bT}$ ). Based upon available experimental data, Cheng and Todreas correlated those boundaries as shown below:

$$\log_{10} \left( \frac{Re_{bL}}{300} \right) = 1.7 \left( \frac{P}{D} - 1.0 \right) \quad (4-14)$$

$$\log_{10} \left( \frac{Re_{bT}}{10000} \right) = 0.7 \left( \frac{P}{D} - 1.0 \right) \quad (4-15)$$

where:  $Re_{bL}$  = laminar-transition Reynolds number  
 $Re_{bT}$  = transition-turbulent Reynolds number  
 $P$  = pin pitch (m)  
 $D$  = pin diameter (m)

The bundle average friction factor can be calculated by accounting for the friction factor constants of each subchannel type and the number of subchannels of each type. That correlation is shown in Equation 4-16. The different constants for laminar and turbulent flow regimes are determined by altering the value of  $m$ , the Reynolds number exponent.

$$C_{fb} = De_b \left[ \sum_{i=1}^3 \frac{N_i A_i}{A_b} \left( \frac{De_i}{De_b} \right)^{m/(2-m)} \left( \frac{C_{fi}}{De_i} \right)^{1/(m-2)} \right]^{m-2} \quad (4-16)$$

where:  $De_b$  = bundle-average equivalent hydraulic diameter  
 $N_i$  = number of each type of subchannel  $i$  in the bundle  
 $A_i$  = axial average flow area in subchannel  $i$   
 $A_b$  = axial bundle-average flow area  
 $De_i$  = equivalent hydraulic diameter of subchannel  $i$   
 $m$  = Reynolds number exponent: 1.0 for laminar, 0.18 for turbulent  
 $C_{fi}$  = friction factor constant for subchannel type  $i$

The friction factors for each type of subchannel,  $C_{fi}$ , are defined in Equations **4-17** through **4-19**. These also apply to both laminar and turbulent flow regimes, depending on the value of  $m$ .

Interior subchannel:

$$C_{f1} = C'_{f1} \left( \frac{P'_{w1}}{P_{w1}} \right) + W_d \left( \frac{3A_{r1}}{A'_1} \right) \left( \frac{De_1}{H} \right) \left( \frac{De_1}{D_w} \right)^m \quad (4-17)$$

Edge subchannel:

$$C_{f2} = C'_{f2} \left[ 1 + W_s \left( \frac{A_{r2}}{A'_2} \right) \tan^2 \theta \right]^{(3-m)/2} \quad (4-18)$$

Corner subchannel:

$$C_{f3} = C'_{f3} \left[ 1 + W_s \left( \frac{A_{r3}}{A'_3} \right) \tan^2 \theta \right]^{(3-m)/2} \quad (4-19)$$

where:  $C'_{fi}$  = bare-rod friction factor constant for subchannel type  $i$   
 $m$  = Reynolds number exponent: 1.0 for laminar, 0.18 for turbulent  
 $P_{w1}$  = interior subchannel wetted perimeter (m)  
 $W_d$  = wire drag constant (see Equation **4-23** and **4-24**)  
 $A_{ri}$  = projected area of wire in a subchannel of type  $i$  (m<sup>2</sup>)  
 $A'_i$  = bare-rod flow area for subchannel of type  $i$  (m<sup>2</sup>)  
 $De_1$  = equivalent hydraulic diameter of interior subchannel (m)  
 $H$  = wire lead length (m)  
 $D_w$  = wire diameter (m)  
 $W_s$  = wire sweeping constant (see Equation **4-21** and **4-22**)  
 $\theta$  = angle between the wire wrap and the vertical axis (radians)

The subchannel friction factor constants depend on three correlated values: the bare-rod friction factor constant  $C'_{fi}$ , the wire-drag constant  $W_d$ , and the wire-sweeping constant  $W_s$ . The bare-rod friction factors are determined by evaluating a quadratic polynomial (Equation **4-20**) with coefficients (Table 2) correlated to experimental data.

$$C'_{fi} = a_0 + a_1 \left( \frac{P}{D} - 1 \right) + a_2 \left( \frac{P}{D} - 1 \right)^2 \quad (4-20)$$

**Table 2. Polynomial factors for bare-rod friction factor constant correlation**

Flow regime	Subchannel	$a_0$	$a_1$	$a_2$
$1.0 \leq P/D \leq 1.1$				
Laminar	Interior	26.00	888.2	-3334
	Edge	26.18	554.5	-1480
	Corner	26.98	1636	-10050
Turbulent	Interior	0.09378	1.398	-8.664
	Edge	0.09377	0.8732	-3.341
	Corner	0.1004	1.625	-11.85
$1.1 \leq P/D \leq 1.5$				
Laminar	Interior	62.97	216.9	-190.2
	Edge	44.40	256.7	-267.6
	Corner	87.26	38.59	-55.12
Turbulent	Interior	0.1458	0.03632	-0.03333
	Edge	0.1430	0.04199	-0.04428
	Corner	0.1499	0.006706	-0.009567

The wire drag and wire sweeping constants,  $W_d$  and  $W_s$ , were calibrated through an iterative process using the database of bundle average friction factor constants and flow split data available in 1984 (except 7-pin results) [24] and are reported for both turbulent and laminar flow regimes.

$$W_{sT} = 20.0 \log \left( \frac{H}{D} \right) - 7.0 \quad (4-21)$$

$$W_{sL} = 0.3W_{sT} = 6.0 \log \left( \frac{H}{D} \right) - 2.1 \quad (4-22)$$

$$W_{dT} = \frac{29.5 - 140 \left( \frac{D_w}{D} \right) + 401 \left( \frac{D_w}{D} \right)^2}{\left( \frac{H}{D} \right)^{0.85}} \quad (4-23)$$

$$W_{dL} = 1.4W_{dT} = \frac{41.3 - 196 \left( \frac{D_w}{D} \right) + 561 \left( \frac{D_w}{D} \right)^2}{\left( \frac{H}{D} \right)^{0.85}} \quad (4-24)$$

#### 4.1.5 Cheng-Todreas Simple (1986)

To simplify the friction factor calculation, Cheng and Todreas proposed simpler empirical correlations to determine the bundle friction factor constant for each flow regime, which are shown in Equations 4-25 and 4-26.

Laminar:

$$C_{fL} = \left[ -974.6 + 1612.0 \left( \frac{P}{D} \right) - 598.5 \left( \frac{P}{D} \right)^2 \right] \left( \frac{H}{D} \right)^{0.06 - 0.085(P/D)} \quad (4-25)$$

Turbulent:

$$C_{fT} = \left[ 0.8063 + 0.9022 \log \left( \frac{H}{D} \right) + 0.3526 \left( \log \left( \frac{H}{D} \right) \right)^2 \right] \left( \frac{P}{D} \right)^{9.7} \left( \frac{H}{D} \right)^{1.78 - 2.0(P/D)} \quad (4-26)$$

The friction factor is evaluated in the same way as for the Cheng-Todreas Detailed correlation, shown in Equations 4-10 through 4-12. The Cheng-Todreas Simple correlation also offers a correlation for the intermittency factor, presented in Equation 4-27.

$$\Psi = \frac{\log(Re_b) - \left( 1.7 \frac{P}{D} + 0.78 \right)}{2.52 - \frac{P}{D}} \quad (4-27)$$

#### 4.1.6 Upgraded Cheng-Todreas (2018)

The 2018 upgrade [17] to the Cheng-Todreas model made three improvements to the 1986 friction factor correlations. First, reexamination of laminar regime friction factor data revealed that the laminar boundary  $Re_{bL}$  should be much lower than that calculated in equation. As a result, the correlation was updated to Equation 4-28.

$$\log\left(\frac{Re_{bL}}{320}\right) = \left(\frac{P}{D} - 1.0\right) \quad (4-28)$$

Second, the equation characterizing the friction factor in the transition flow regime was modified (initially published in [25]) to replace Equation 4-12; the new equation is shown in Equation 4-29, where  $f_{bT}$ ,  $f_{bL}$ , and  $\Psi_b$  are the bundle turbulent and laminar friction factors and intermittency factor.

$$f_{btr} = f_{bT}\Psi^{1/3} + f_{bL}(1 - \Psi_b)^{1/3}(1 - \Psi_b^\lambda) \quad (4-29)$$

where:  $\lambda$  = calibration constant (taken to be 7).

The third improvement was the revision of the wire drag constant,  $W_d$ , and wire sweeping constant,  $W_s$ , to correct the effect of pin number of the pressure drop prediction. These constants have been revised to the following:

$$W_{sT} = -11.0 \log\left(\frac{H}{D}\right) + 19.0 \quad (4-30)$$

$$W_{sL} = W_{sT} \quad (4-31)$$

$$W_{dT} = \frac{19.56 - 98.71\left(\frac{D_w}{D}\right) + 303.47\left(\frac{D_w}{D}\right)^2}{\left(\frac{H}{D}\right)^{0.541}} \quad (4-32)$$

$$W_{dL} = 1.4W_{dT} \quad (4-33)$$

## 4.2 Flow split

Flow split parameters characterize the flow in the individual subchannels relative to the flow in the overall bundle. Conceptually, the flow split  $X$  is equal to the ratio of the axial velocity of flow through a subchannel to the overall bundle-average axial velocity. Flow split parameters are defined for each type of subchannel: interior ( $X_1$ ), edge ( $X_2$ ), and corner ( $X_3$ ). The correlations for flow split parameters are intertwined with those for friction factor. As noted earlier, the Novendstern correlation for friction factor depended on flow split; by contrast, the Cheng-Todreas correlation for flow split depends on constants defined as part of the friction factor correlations. The flow split is constant for a given bundle geometry and flow regime.

### 4.2.1 Novendstern (1972)

Novendstern [20] defined the flow split between the interior subchannels and the edge and corner subchannels as a function of the geometric properties of the bundle. Equation 4-34 shows the equation for the flow split parameter for the interior subchannels; the parameters for edge and corner subchannels can be found using similar expressions.

$$X_1 = A_T \left[ N_1 A_1 + N_2 A_2 \left( \frac{De_2}{De_1} \right)^{0.714} + N_3 A_3 \left( \frac{De_3}{De_1} \right)^{0.714} \right]^{-1} \quad (4-34)$$

where:  $A_T$  = total flow area (m<sup>2</sup>)  
 $N_i$  = number of subchannels of type  $i$   
 $A_i$  = flow area (m<sup>2</sup>) of subchannel type  $i$   
 $De_i$  = equivalent hydraulic diameter (m) of subchannel type  $i$

### 4.2.2 MIT Chiu-Todreas-Rohsenow (1980)

Based on available experimental data at the time, a group at MIT characterized [16] the flow split parameters in terms of bundle geometry. They sought to improve on the method proposed by Novendstern and that was used in COBRA-III C, which were described as somewhat deficient in the prediction of the effect of wire lead on the flow split parameters. Parameters for interior and edge subchannels were proposed; those for the corner were assumed to be like those for the edge with negligible overall impact because the corner subchannel flow



has only a small effect on overall flow distribution if the number of pins in the bundle is greater than 61. These are the flow split correlations that were ultimately built into SUPERENERGY-2.

$$X_1 = \frac{A_1 N_1 + A_2 N_2 + A_3 N_3}{A_1 N_1 + G^{0.571} \left( \frac{D_{e2}}{D_{e1}} \right)^{0.714} [A_2 N_2 + A_3 N_3]} \quad (4-35)$$

$$X_2 = \frac{A_1 N_1 + A_2 N_2 + A_3 N_3}{A_1 N_1 G^{-0.571} \left( \frac{D_{e1}}{D_{e2}} \right)^{0.714} + A_2 N_2 + A_3 N_3} \quad (4-36)$$

where:  $A_i$  = flow area (m<sup>2</sup>) of subchannel type  $i$   
 $N_i$  = number of subchannels of type  $i$   
 $G$  = constant based on bundle geometry  
 $De_i$  = equivalent hydraulic diameter (m) of subchannel type  $i$

These equations both rely on  $G$ , a constant based on correlated constants calibrated based on available experimental data and bundle geometry characteristics.  $G$ , and the other values on which it relies, are reported below.

$$G = \frac{2200 \left( \frac{D_{e1}}{H} \right) \left( \frac{A_{r1}}{A'_1} \right) \left[ \frac{P}{(\pi^2 P^2 + H^2)^{0.5}} \right]^2 + 1}{1.2 \left[ 1 + \left( 1.9n \frac{V_T}{V_2} \Big|_{\text{gap}} \right)^2 \right]^{1.375}} \quad (4-37)$$

$$n = \frac{d_{\text{gap}} P}{2 \left[ \left( \frac{D}{2} + d_{\text{gap}} \right) \frac{P}{2} - \frac{\pi D^2}{16} \right]} \quad (4-38)$$

$$\frac{V_T}{V_2} \Big|_{\text{gap}} = 10.5 \left( \frac{D_w}{P} \right)^{0.35} \frac{P}{(\pi^2 P^2 + H^2)^{0.5}} \left( \frac{A_{r2}}{A'_2} \right)^{0.5} \quad (4-39)$$

where:  $De_i$  = equivalent hydraulic diameter (m) of subchannel type  $i$   
 $H$  = wire wrap lead (m)  
 $A_{ri}$  = projected wire wrap area into flow area (m<sup>2</sup>) of subchannel type  $i$   
 $A'_i$  = bare rod flow area (m<sup>2</sup>) of subchannel type  $i$   
 $P$  = pin pitch (m)

$d_{\text{gap}}$  = distance between edge pin outer clad and duct wall (m)  
 $D$  = pin diameter (m)  
 $D_w$  = wire wrap diameter (m)

#### 4.2.3 Cheng-Todreas (1986)

The Cheng-Todreas flow-split correlation [14] defines three values, one for each type of subchannel. Evaluation of flow split ratios in Equations 4-41 and 4-42 allows solution of the flow split parameter for the edge subchannel in Equation 4-40, from which the other flow split parameters can be evaluated. Like the Novendstern flow split definition, the Cheng-Todreas flow split distributions are a function of the bundle geometry. The friction factor constants (see Section 4.1.4) are themselves functions of bundle geometry.

$$X_2 = \left( \frac{N_2 A_2}{A_b} + \left( \frac{X_1}{X_2} \right) \frac{N_1 A_1}{A_b} + \left( \frac{X_3}{X_2} \right) \frac{N_3 A_3}{A_b} \right) \quad (4-40)$$

$$\frac{X_1}{X_2} = \left( \frac{De_1}{De_2} \right)^{(1+m)/(2-m)} \left( \frac{C_{f2}}{C_{f1}} \right)^{1/(2-m)} \quad (4-41)$$

$$\frac{X_3}{X_2} = \left( \frac{De_3}{De_2} \right)^{(1+m)/(2-m)} \left( \frac{C_{f2}}{C_{f3}} \right)^{1/(2-m)} \quad (4-42)$$

where:  $X_i$  = flow-split parameter for subchannel  $i$   
 $N_i$  = number of each type of subchannel  $i$  in the bundle  
 $A_i$  = axial average flow area in subchannel  $i$   
 $A_b$  = axial bundle-average flow area  
 $De_i$  = equivalent hydraulic diameter of subchannel  $i$   
 $C_{fi}$  = friction factor constant for subchannel  $i$  (see Section 4.1.4)  
 $m$  = Reynolds number exponent; 1.0 for laminar, 0.18 for turbulent

### 4.3 Mixing parameters

DASSH uses two mixing parameters, eddy diffusivity and swirl velocity, in the interior and exterior regions of the bundle, respectively, to account for transverse convective heat

transfer caused by the wire wraps without solving the coupled heat and momentum equations. The past research on these parameters is largely attributed to Todreas and his colleagues' work on the ENERGY family of codes, on which DASSH is based.

#### 4.3.1 Chiu, Rohsenow, and Todreas (1978)

Chiu, Rohsenow, and Todreas [16] recorelated the mixing parameters that were built into the original ENERGY and SUPERENERGY codes based on an expanded database of experimental data. They used the local subchannel velocity as a nondimensionalizing parameter, which made the resulting correlation independent of bundle size. These are the correlations for mixing parameters built into SUPERENERGY-2. The correlations for eddy diffusivity and swirl velocity are shown in Equations 4-43 and 4-44, respectively.

$$\varepsilon_{1\eta}^* = 0.128 \left( \frac{P}{P-D} \right)^{0.5} \left( \frac{A_{r1}}{A_1} \right)^{0.5} \frac{(D + D_w)P^2}{A_1(\pi^2(D + D_w)^2 + H^2)^{0.5}} \quad (4-43)$$

$$C_{1L} = 10.5 \left( \frac{P-D}{P} \right)^{0.35} \left( \frac{A_{r2}}{A_2} \right)^{0.5} \frac{D + D_w}{(\pi^2(D + D_w)^2 + H^2)^{0.5}} \quad (4-44)$$

where:  $P$  = pin pitch (m)  
 $D$  = pin diameter (m)  
 $A_{ri}$  = projected area (m<sup>2</sup>) of wire in subchannel type  $i$   
 $A_i$  = axial flow area (m<sup>2</sup>) in subchannel type  $i$   
 $D_w$  = wire wrap outer diameter (m)  
 $H$  = wire wrap lead (m)

#### 4.3.2 Cheng-Todreas (1986)

Cheng and Todreas [14] derived separate mixing parameter correlations for laminar (L) and turbulent (T) regimes; mixing parameters  $\phi$  in the transition regime are determined based on Equation 4-45, where  $\Psi$  is a modified version of the intermittency factor defined in Equation 4-13; in this case, the intermittency factor is defined for each subchannel type in order to obtain subchannel-specific mixing parameters. The exponent  $\gamma$  is a constant obtained through fitting experimental data (taken to be 2/3).

$$\phi = \phi_L + (\phi_T - \phi_L)\Psi_i^Y \quad (4-45)$$

$$\Psi_i = \frac{\log Re_i - \log \left( Re_{bL} X_{iL} \left( \frac{D_{ei}}{D_{eb}} \right) \right)}{\log \left( Re_{bT} X_{iT} \left( \frac{D_{ei}}{D_{eb}} \right) \right) - \log \left( Re_{bL} X_{iL} \left( \frac{D_{ei}}{D_{eb}} \right) \right)} \quad (4-46)$$

where:  $Re_i$  = Reynolds number in subchannel type  $i$   
 $Re_{bL}$  = laminar-transition Reynolds number  
 $Re_{bT}$  = transition-turbulent Reynolds number

The eddy diffusivity (mixing parameter for the interior region) is defined as:

$$\varepsilon_{1\eta}^* = C_m (A_{r1}/A'_1)^{1/2} \tan \theta \quad (4-47)$$

where:  $C_m$  = empirical constant depending on flow regime and geometry  
 $A_{r1}$  = projected area of wire in an interior subchannel (m<sup>2</sup>)  
 $A'_1$  = bare-rod axial flow area in an interior subchannel (m<sup>2</sup>)  
 $\theta$  = angle between the wire wrap and the vertical axis (radians)

Note that if the wire wrap is not “wrapped” and just runs straight up the pin,  $\theta = 0$  such that  $\tan \theta = 0$  and there is no enhanced eddy diffusivity to promote transverse heat transfer. The empirical constant in Equation 4-47 is defined for the turbulent and laminar regions.

Turbulent Region

Laminar Region

$$N_r \geq 19: C_{mT} = 0.14(c/D)^{-1/2} \quad (4-48)$$

$$N_r \geq 19: C_{mL} = 0.077(c/D)^{-1/2} \quad (4-49)$$

$$N_r = 7: C_{mT} = 0.1(c/D)^{-1/2} \quad (4-50)$$

$$N_r = 7: C_{mL} = 0.055(c/D)^{-1/2} \quad (4-51)$$

where:  $c$  = gap between pins (m)  
 $D$  = pin diameter (m)  
 $N_r$  = number of pins in the bundle

The swirl velocity (mixing parameter for the edge region) is defined as:

$$C_{1L} = C_s (A_{r2}/A'_2)^{1/2} \tan \theta \quad (4-52)$$

where:  $C_s$  = empirical constant depending on flow regime and geometry  
 $A_{r2}$  = projected area of wire in an edge subchannel (m<sup>2</sup>)  
 $A'_2$  = bare-rod axial flow area in an edge subchannel (m<sup>2</sup>)  
 $\theta$  = angle between the wire wrap and the vertical axis (radians)

The empirical constant in Equation 4-52 is defined separately for the turbulent and laminar regions.

Turbulent Region

Laminar Region

$$N_r \geq 19: C_{sT} = 0.75(H/D)^{0.3} \quad (4-53)$$

$$N_r \geq 19: C_{sL} = 0.413(H/D)^{0.3} \quad (4-54)$$

$$N_r = 7: C_{sT} = 0.6(H/D)^{0.3} \quad (4-55)$$

$$N_r = 7: C_{sL} = 0.33(H/D)^{0.3} \quad (4-56)$$

#### 4.4 Heat transfer coefficient

The heat transfer coefficients for convection between (1) coolant and duct wall, and (2) coolant and pins are calculated based on the Nusselt number, as shown below in a general form.

$$h = \frac{k \text{Nu}_i}{D_e} \quad (4-57)$$

where:  $h$  = heat transfer coefficient (W/m<sup>2</sup>K)  
 $k$  = coolant thermal conductivity (W/m-K)  
 $\text{Nu}$  = Nusselt number  
 $D_e$  = hydraulic diameter (m)

The Dittus-Boelter correlation, shown below, is used to calculate the Nusselt number. The correlation enables the determination of Nusselt number for a specific subchannel type or for the bundle average, depending on the value of the Reynolds number used. The constants A, B, C, and D are correlation coefficients that can be input by the user.

$$\text{Nu}_i = A * (\text{Re}_i^B \text{Pr}^C) + D \quad (4-58)$$

where:  $Re_i$  = Reynolds number of subchannel type  $i$  or bundle average  
 $Pr$  = Prandtl number of coolant, at bundle average temperature

For convection with the duct wall, the default values for A, B, C, and D are 0.025, 0.8, 0.8, and 7.0, respectively, as given by the Lyon-Martinelli equation [26] [27] [28]; a review of other correlations for Nusselt number for convection with walls is given in Ref. [29] .

For convection between coolant and pins, the default coefficients are calculated based on pin geometry parameters, as shown below.

$$A = \frac{1}{3} \left( \frac{P}{D} \right)^{3.8} 0.01^{0.86} \quad (4-59)$$

$$B = C = 0.86 \quad (4-60)$$

$$D = 4.0 + 0.16 \left( \frac{P}{D} \right)^5 \quad (4-61)$$

where:  $P$  = pin pitch (m)  
 $D$  = pin diameter (m)

#### 4.5 Fuel thermal conductivity

For metallic fuel, the thermal conductivity is evaluated based on the correlation developed in Ref. [30], as shown in Equations 4-62 through 4-66. Capability for non-metallic fuel thermal conductivity evaluation may be implemented in the future.

$$k_f = x_p [A + BT + CT^2] \quad (4-62)$$

$$A = 17.5 \left[ \frac{1 - 2.23W_{Zr}}{1 + 1.61W_{Zr}} - 2.62W_{Pu} \right] \quad (4-63)$$

$$B = 0.0154 \left[ \frac{1 + 0.061W_{Zr}}{1 + 1.61W_{Zr}} + 0.90W_{Pu} \right] \quad (4-64)$$

$$C = 9.38 \times 10^{-6}(1 - 2.70W_{Pu}) \quad (4-65)$$

$$x_p = \frac{1 - Po}{1 + \beta Po} \quad (4-66)$$

where:  $T$  = fuel temperature (K)  
 $W_{Zr}$  = weight fraction Zr in fuel  
 $W_{Pu}$  = weight fraction Pu in fuel  
 $Po$  = fuel porosity fraction (no porosity if equal to 0.0)  
 $\beta$  = calibration constant, taken equal to 2.0

## 5 Power distributions

A fundamental component of the DASSH calculation is the power distribution. The quality of the power distribution has a direct impact on the quality of the solution. The SE2-ANL requirement to use power distributions obtained from DIF3D-FD was a primary motivation behind the development of DASSH. Additionally, one of the major simplifications in SE2-ANL is that it assumes the radial power distribution in each assembly does not change axially over a given DIF3D mesh. By contrast, DASSH allows the full three-dimensional shape of the power to be correctly applied to all assemblies and divided among pins, ducts, and coolant.

DASSH stores power distributions (W/m) in the form of 1-D polynomials in  $z$  for each pin, duct element, and coolant subchannel. The axial space may be subdivided into power-regions that are distinct from the axial regions described in Section 3.12.3. Each axial power-region has its own set of power-distribution polynomials. The element reference space of each axial power-region is -0.5 cm to 0.5 cm. During the axial sweep, DASSH takes the midpoint between axial planes  $j$  and  $j + 1$  and scales it into the element reference space. Then, the 1-D polynomials for linear power are evaluated. This approach constitutes a midpoint rule to defining the total power in the assembly and it requires proper normalization to avoid power errors.

The following subsections describe how power distributions are obtained from ARC binary files and user text-based input. Couplings to neutronics codes other than ARC may be pursued in the future.

### 5.1 *Obtaining power distributions from ARC: VARPOW*

This subsection describes the process by which DASSH obtains polynomial power distributions from ARC binary files. Detailed descriptions of the ARC codes [3] and the binary files they use are not provided. Interested users should consult the relevant literature, such as the DIF3D-VARIANT [5] and GAMSOR [8] user manuals, for more information.



The result of running GAMSOR are binary files (of the NHFLUX and/or NHFLX0 form) containing polynomial coefficients that characterize the neutron and gamma fluxes in the reactor. These binary files, along with those for the geometry (GEODST), model labels (LABELS), material atom densities (ZNATDN), and material isotopic content (NDXSRF) are needed. To include gamma heating, the neutron and gamma heating cross sections (PMATRX) and neutron/gamma flux solutions from GAMSOR are needed. All of these files are processed by a utility program in ARC, named VARPOW, which produces the material-based power distribution information used by DASSH. Based on user specification of the fuel type and coolant material, VARPOW divides power among fuel, structural, and coolant materials according to the isotopic atomic weight ranges shown in Table 3. Although this method may misclassify some isotopes that are included in the range but do not belong to the group, the impact on the result should be small.

**Table 3. VARPOW material classification**

	Type	Atomic weight range (amu)
Fuel type	Zr-alloyed metal fuel	89.5 – 96.0
	Oxide fuel	15.5 – 18.1
	Nitride fuel	13.9 – 15.1
	Aluminum fuel	26.5 – 27.0
Coolant type	Sodium	22.5 – 23.0
	Sodium-potassium	22.5 – 23.0; 38.5 – 41.0
	Lead or lead-bismuth	203.5 – 210.0
	Tin (Sn)	111.5 – 124.0
Structure (clad, duct)	Cr, Mn, Fe, Co, Ni, Cu	49.0 – 65.0
	Mo	91.5 – 100.0

The distribution of power among fuel, structure, and coolant is carried out as follows. First, fuel-alloying isotopes are classified as belonging to fuel. For example, the atomic weight range from 89.5-96.0 amu is used to classify Zr isotopes as fuel if Zr-alloyed metal fuel is selected. Alternatively, if oxide fuel is selected, oxygen isotopes are grouped as fuel using the range 15.5-18.1 amu. Next, isotopes corresponding to the user-specified coolant type are classified as coolant. Then, structural materials are identified based on an atomic weight range that includes a fixed set of isotopes: Cr, Mn, Fe, Co, Ni, Cu, and Mo. Finally, all remaining isotopes are classified as fuel.

With these material classifications, VARPOW combines heating factors and neutron and gamma flux data to produce neutron and gamma power densities ( $\text{W}/\text{cm}^3$ ) in each type of material for all DIF3D meshes. Additionally, VARPOW transforms the coefficients in the NHFLUX files from a polynomial basis to a monomial basis for ease-of-use in DASSH. VARPOW provides the m, n, and o monomial exponent values ( $x^m y^n z^o$ ) associated with the power distribution expansion it produces.

Using the computed centroid coordinates (x,y) for each pin, duct mesh, and coolant channel, DASSH evaluates the neutron and gamma monomial coefficients and exponents at the targeted coordinate to produce an axial power shape (as a one-dimensional polynomial in z) for each. The neutron and gamma distributions are scaled by the material power densities and added together to obtain the combined power distributions in the pins, duct, and coolant. Because the (x,y) point evaluation does not constitute an exact integral in the x-y space, the polynomials are renormalized within each DIF3D mesh to produce the correct total power for that mesh.

## **5.2 User-specified power distributions**

The user may specify power distributions for input to DASSH. These are passed to DASSH by way of a CSV file that contains the power profile coefficients (for a polynomial in z) for each pin, duct, and coolant mesh in each assembly. After performing input checks and conducting any requested renormalization, DASSH uses these power distributions directly.

The structure of the CSV is shown in Table 4. The axial boundaries input to columns 3 and 4 are absolute axial positions in the assembly, between which the power distribution applies. The power distribution axial region definitions must be the same for all pins, duct elements, and coolant subchannels. No gaps or overlaps are allowed between regions. The coefficients input in columns 6+ are for polynomials on the  $[-0.5, 0.5]$  basis. Because this length basis is unitless, all should have units of  $\text{W}/\text{m}$ . The coefficients are zero by default; for example, for the user to specify a power distribution with no power distributed to the duct or coolant in a particular assembly, they may omit those rows from the CSV.

**Table 4. CSV structure for user-specified power distributions in DASSH**

Column	Value
1	Assembly ID
2	Material type (for pin, =1; if duct, =2; if coolant, =3)
3	Lower z-boundary (m)
4	Upper z-boundary (m)
5	Material ID (e.g. pin, duct element, or coolant subchannel index)
6	0 <sup>th</sup> -order polynomial coefficient $a_0$ (for use as $a_0 z^0$ )
7	1 <sup>st</sup> -order polynomial coefficient $a_1$ (for use as $a_1 z^1$ )
8	2 <sup>nd</sup> -order polynomial coefficient $a_2$ (for use as $a_2 z^2$ )
9+	Higher-order polynomial coefficients

User-specified power distributions may be used alongside power distributions obtained from DIF3D. When both inputs are provided, the power distribution from DIF3D is processed first, then overwritten where user-defined power distributions are specified. This is useful for situations in which the DIF3D power distribution is inaccurate in a particular assembly or core region.

## 6 DASSH code calculation procedure

DASSH is organized as a hierarchy of code objects. Figure 20 shows the organization of the main objects in DASSH. These objects are listed and briefly described in Table 5

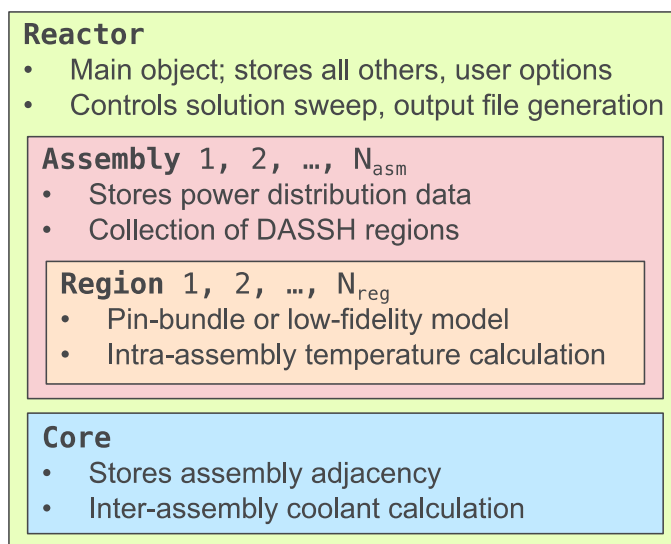


Figure 20. Organization of main code objects in DASSH

Table 5. Main DASSH objects relevant to code execution

Object	Container	Description
Reactor	None	<ul style="list-style-type: none"> <li>• The primary container for DASSH objects</li> <li>• Controls the temperature sweep calculation</li> </ul>
Core	Reactor	<ul style="list-style-type: none"> <li>• Contains core map, assembly adjacency, and methods to calculate inter-assembly gap temperatures</li> </ul>
Assembly	Reactor	<ul style="list-style-type: none"> <li>• Contains assembly identifiers, coolant and duct temperatures and calculation methods</li> <li>• Contains set of distinct axial regions</li> <li>• One instance for every assembly in the core</li> </ul>
AssemblyPower	Assembly	<ul style="list-style-type: none"> <li>• Holds pin, duct, and coolant power distributions; called by Assembly object throughout sweep</li> </ul>
RoddedRegion	Assembly	<ul style="list-style-type: none"> <li>• Parameters and methods characterizing pin bundle geometry and calculate intra-assembly temperatures</li> </ul>
UnroddedRegion	Assembly	<ul style="list-style-type: none"> <li>• Specific parameters and methods for the low-fidelity model system.</li> </ul>

The highest-level object in DASSH is the Reactor object, which contains the other objects and controls the temperature sweep calculation. The Reactor object stores a set of Assembly objects, one for each assembly in the core. These contain the power distribution information and a set of DASSH Region objects that differentiate the axial regions (see Section 3.12.3) of the assembly. Because the Regions are defined by different geometric parameters that affect the temperature calculation (e.g. a pin-bundle or porous media parameters for the low-fidelity model), the intra-assembly temperature calculation takes place in the Region object. For example, this includes the temperature calculation among coolant subchannels in the pin bundle. Additionally, the Reactor object stores the Core object, which in turn stores the assembly adjacency and controls the calculation of the inter-assembly gap coolant temperatures.

This section describes the DASSH calculation procedure, beginning with input processing and culminating with output file preparation. For information about preparing input files, please see the DASSH user guide [7].

### **6.1 Reading input, problem setup**

DASSH utilizes the Python package ConfigObj [31] to read input files. It internally checks input arguments against values and types codified in the DASSH template files. DASSH relies on these checks, as well as others built into the input processing routine, to ensure that all necessary user input is present, intelligible, and satisfies logical, geometric, and physical constraints. If the input is accepted, DASSH produces an object containing the input data to be used to initialize the main code objects. In the process, the units of all user inputs are converted from the user-specified units to DASSH native units (length: m; temperature: K; mass flow rate: kg/s).

The Reactor object is the main DASSH code object; in the process of creating the Reactor object, all others are created within it based on user input. Most crucially, this includes (1) processing power distributions from user input or ARC binary files, (2) calculation of parameters that characterize pin bundle geometries, and (3) assignment of geometry parameters, power distributions, and coolant flow to assemblies. The following enumerates the procedure

of instantiating the Reactor object; once it has been created, the temperature sweep can be initiated.

1. Power distribution data is generated based on user-provided ARC binary files (by running VARPOW) or is imported from user input. This data is further processed into assembly component power distributions in a later step
2. Assembly geometry and pin bundle characteristics are instantiated in Assembly object templates based on user specification.
3. Power distributions for pins, duct, and coolant are generated for each assembly. If the user has provided their own CSV-input for power in part of that assembly, it overrides the distribution that might otherwise be obtained from any provided ARC binary files. The total core power is scaled according to user input.
4. With power distributions generated for each assembly and the inlet coolant temperature condition known, coolant mass flow rates are assigned to each assembly. If the user has assigned coolant mass flow rate in the input, no further processing is necessary. If the user has specified the assembly coolant outlet temperature or temperature rise, DASSH estimates the required coolant flow rate to achieve that condition based on  $Q = mC_p dT$ , with an average coolant heat capacity, assuming no heat transfer between assemblies.
5. The calculated power distributions and mass flow rate are used to create Assembly objects, one for each assembly in the core. DASSH calculates the limiting axial mesh size requirement for each assembly.
6. The Core object – which controls assembly adjacency and inter-assembly heat transfer – is instantiated. The coolant flow rate through the inter-assembly gap is calculated based on user input specifying the fraction of core total flow rate that flows through the inter-assembly gap (e.g. if 100 kg/s is allotted to the assemblies and the gap fraction is 0.0099, the inter-assembly gap flow rate is 101.0). The axial mesh size requirement of the inter-assembly gap coolant is determined.
7. The axial region boundaries from the power distributions and assembly specifications are combined to form a set of axial points where solutions are required. These, along

with the overall limiting axial mesh size requirement, are used to generate the axial points at which temperatures are evaluated throughout the sweep.

8. Objects to which dumped temperature data is written are created, as necessary.

## **6.2 Solution sweep procedure**

DASSH calculates temperatures throughout the core by stepping from each predetermined axial plane to the next. The algorithm describing the solution execution is shown in Figure 21. At the beginning, all temperatures are known because the user provides the core inlet temperature. Coolant temperatures in each assembly and in the inter-assembly gap are fixed by user input, and duct temperatures at the inlet are computed based on inlet coolant temperatures. to balance energy among the inlet temperatures.

Each axial step begins with the calculation of inter-assembly gap coolant temperatures. Duct surface temperatures are obtained from every assembly on the inter-assembly gap mesh, resolving mesh disagreements where necessary. These are used by the Core object, along with the inter-assembly gap coolant temperatures from the previous axial step, to determine the coolant temperatures at the next step.

Once the inter-assembly gap temperatures are known, DASSH loops over all Assembly objects to compute temperatures coolant and duct temperatures. The assembly calculation starts with assessing whether the step occurs in a new axial region (see Section 3.12.3) and updating to a new Region object if necessary. The pressure drop across the axial step is calculated. Then, the linear power in the pins, duct, and coolant (or the average linear power if in a low-fidelity region) is determined. The pin and coolant (or average) power is distributed to the coolant subchannels in the calculation of coolant temperatures, which also relies on coolant and duct temperatures from the previous step. Once all coolant temperatures are known, the duct temperatures are solved. The duct temperature calculation requires as input the just-solved inter-assembly gap coolant temperatures adjacent to the assembly, which are projected to the duct mesh as necessary. Finally, with all coolant temperatures solved at the current axial plane, pin temperatures are calculated if requested, using the average temperature of the surrounding coolant subchannels as an external boundary condition.

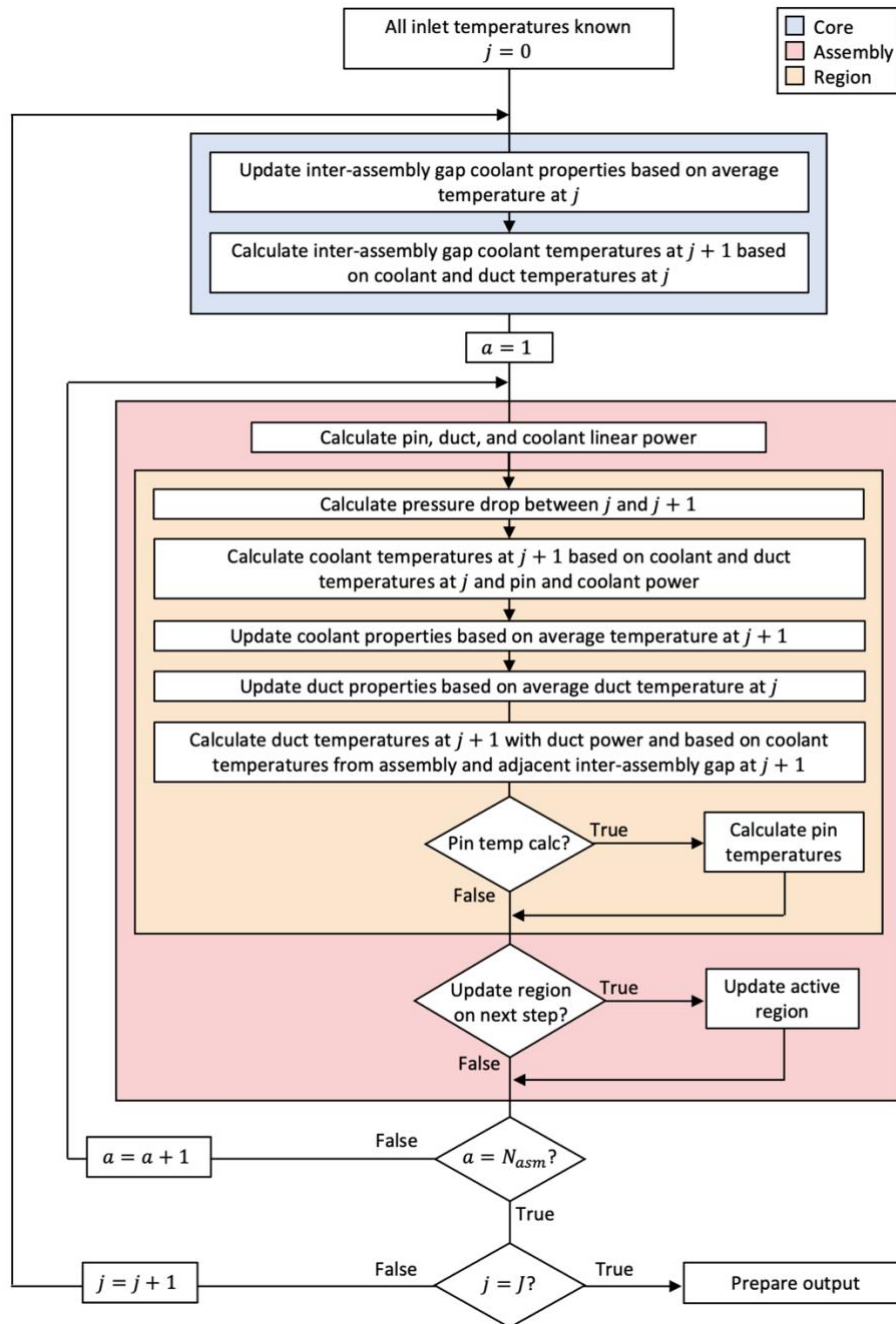


Figure 21. DASSH sweep algorithm flowchart

This process continues until DASSH has swept through the entire axial space. At the end of the calculation, DASSH updates the summary output file with results. Throughout the sweep, each Assembly tracks the peak coolant, duct, and pin temperatures observed to be reported in the summary output. Each Region object also tracks the coolant energy balance,



monitoring energy addition by heat generation and cumulative energy addition and removal by heat transfer through the duct walls. DASSH also monitors the energy balance on the inter-assembly coolant. All these results are recorded in the summary output file.

### 6.3 DASSH output

The primary DASSH output is the summary output, recorded in a file called “dassh.out”. DASSH always generates this output file. There, multiple tables provide an overview of temperatures throughout the core. There can be up to nine sections, described below in Table 6.

**Table 6. Description of summary output file tables**

ID	Table name	Description
1	Pin bundle geometry summary	<ul style="list-style-type: none"> <li>Pin bundle overview for each defined assembly type</li> <li>Subchannel characteristics and assigned correlations</li> </ul>
2	Assembly power and assigned flow rate	<ul style="list-style-type: none"> <li>Position, total power, and total flow rate for each assembly</li> <li>Axial step size constraint and the constraining subchannel</li> <li>Applicability of forced convection assumption (modified Gr)</li> </ul>
3	Subchannel flow characteristics	<ul style="list-style-type: none"> <li>Average and individual subchannel velocities</li> <li>Correlated parameters for each assembly at inlet temperature</li> <li>Note: these values will change throughout the sweep as coolant properties change with increasing temperature.</li> </ul>
4	Pressure drop across assemblies	<ul style="list-style-type: none"> <li>Pressure drop across each axial region</li> <li>Total pressure drop across the assembly</li> </ul>
5	Overall assembly energy balance	<ul style="list-style-type: none"> <li>Optional depending on user input</li> <li>Coolant energy balances for each assembly</li> </ul>
6	Inter-assembly energy balance	<ul style="list-style-type: none"> <li>Optional depending on user input</li> <li>Energy transferred through the inter-assembly gap coolant arranged by duct hex face for each assembly</li> </ul>
7	Assembly coolant temperature summary	<ul style="list-style-type: none"> <li>Assembly coolant average and peak outlet temperatures</li> <li>Overall peak coolant temperature in any subchannel (tracked throughout sweep) and the axial height at which it occurs</li> </ul>
8	Assembly duct temperature summary	<ul style="list-style-type: none"> <li>Average duct temperature at outlet for each hex face</li> <li>Overall peak duct temperature in any duct element (tracked throughout sweep) and the axial height at which it occurs</li> </ul>
9	Peak pin temperatures	<ul style="list-style-type: none"> <li>Pin temperatures (coolant, clad, fuel) at height of peak clad mid-wall temperature; reported for pin in which peak temperature occurs</li> <li>Pin temperatures (coolant, clad, fuel) at height of peak fuel centerline temperature; reported for pin in which peak temperature occurs</li> </ul>

DASSH writes the first three tables in the output file at the start of the calculation. This gives users the opportunity to study Table 2 (which reports the axial mesh size constraint and limiting subchannel for each assembly) early in the calculation. This may inform modifications to the assembly geometry, boundary conditions, or assumptions that need to be made to accelerate the calculation.

The remaining tables in the output file are written at the end of the calculation, after the axial sweep. These summary results provide general design-basis information such as average and peak coolant and duct temperatures and radial pin temperature profiles at the locations of peak clad and peak fuel temperature.

If requested by the user, DASSH will dump temperature data throughout the axial sweep. The data is written to CSV files in the DASSH working directory. Because these temperatures are organized by subchannel, they are best processed via DASSH, which already has the capability to map them. The primary use for these files is the built-in visualization capability included in DASSH. For users who need to perform their own data analysis, the format of these files is described in the DASSH user guide.

## 7 Conclusions

DASSH is a steady-state subchannel thermal hydraulics code for hexagonally gridded reactor cores with ducted assemblies. It calculates pressure drop in the assemblies and temperatures in the coolant, ducts, and pins based on an assigned coolant mass flow rate, accounting for inter-assembly heat transfer. DASSH is intended for use as part of the reactor design process to provide a rapid assessment of the flow and temperature distribution, especially when the assembly design is not fully developed in the early stages of the design process. DASSH is integrated with the ARC code suite to obtain detailed 3-D power distributions in the pins, duct, and coolant based on neutron transport simulation results.

DASSH builds on the methodology featured in SE2-ANL, which calculates energy balances between subchannels and relies on correlations to avoid solving coupled energy and momentum equations. In DASSH, the models have been reformulated, removing approximations where possible. This theory manual presents the derivation of these energy balance models and the constraints that are required for numerical stability. A review of the relevant correlations available for use in DASSH is included as well, along with a description of the power distribution generation process and the DASSH execution procedure.

DASSH is under development and new capabilities will be released soon. Of particular significance is the capability to determine flow orificing groups and optimize flow rates to meet user-defined constraints. With this capability, DASSH will formalize a critical component of reactor design. Additionally, alternative methods of power distribution input may be developed to couple DASSH to other neutronics codes such as OpenMC.

This document is one of a few on DASSH. Descriptions of the installation procedure, input file formatting, and output file generation and processing are provided in the DASSH User Guide. A report on DASSH benchmarking against experiment and other simulations is in preparation. Further documentation may be released in the future as DASSH undergoes verification and validation.

## 8 References

- [1] W. S. Yang, *Fortran 77 Version of SE2-ANL*, Argonne National Laboratory, 1993.
- [2] K. L. Basehore and N. E. Todreas, "SUPERENERGY-2: A multiassembly, steady-state computer code for LMFBR core thermal-hydraulic analysis," 1980.
- [3] Argonne National Laboratory, "Reactor Physics and Fuel Cycle Analysis Software," 2020. [Online]. Available: <http://www.ne.anl.gov/capabilities/rpfca/codes/index.html>. [Accessed 2020 17 August].
- [4] B. V. Richard, "Reactor Hot Spot Analysis," FRA-TM-152, Argonne National Laboratory, 1985.
- [5] G. Palmiotti, E. Lewis and C. Carrico, "VARIANT: VARIational Anisotropic Nodal Transport for Multidimensional Cartesian and Hexagonal Geometry Calculations," ANL-95/40, Argonne National Laboratory, 1995.
- [6] K. L. Derstine, "DIF3D - A Code to Solve One-, Two-, and Three-Dimensional Finite-Difference Diffusion Theory Problems," ANL-82-64, Argonne National Laboratory, 1984.
- [7] M. Atz, M. A. Smith and F. Heidet, "Ducted Assembly Steady State Heat transfer software (DASSH) - User Guide," ANL/NSE-21/34, Argonne National Laboratory, 2021.
- [8] M. A. Smith, C. Lee and R. N. Hill, "GAMSOR: Gamma Source Preparation and DIF3D Flux Solution," ANL/NE-16/50, Argonne National Laboratory, 2016.
- [9] E. U. Khan, W. M. Rohsenow, A. A. Sonin and N. E. Todreas, "A porous body model for predicting temperature distribution in wire-wrapped fuel rod assemblies," *Nuclear Engineering and Design*, vol. 35, pp. 1-12, 1975.
- [10] H. L. Beckers, "Heat transfer in turbulent tube flow," *Applied Scientific Research, Section A*, vol. 6, pp. 147-190, 1956.
- [11] E. U. Khan, W. M. Rohsenow, A. A. Sonin and N. E. Todreas, "A Porous Body Model For Predicting Temperature Distributions In Wire Wrapped Fuel and Blanket Assemblies of a LMFBR," COO-2245-16TR, Massachusetts Institute of Technology, Cambridge, Massachusetts, 1975.
- [12] D. J. Zigrang and N. D. Sylvester, "A Review of Explicit Friction Factor Equations," *Journal of Energy Resources Technology*, vol. 107, no. 2, pp. 280-283, 1985.
- [13] The RELAP5 Development Team, RELAP5/MOD3 Code Manual - Code Structure, System Models, and Solution Methods, vol. 1, NUREG/CR-5535, INEL-95/0174, Idaho National Laboratory, 1995.
- [14] S.-K. Cheng and N. E. Todreas, "Hydrodynamic models and correlations for bare and wire-wrapped hexagonal rod bundles - bundle friction factors, subchannel friction factors and mixing parameters," *Nuclear Engineering and Design*, vol. 92, pp. 227-251, 1986.
- [15] N. E. Todreas and M. S. Kazimi, *Nuclear Systems II - Elements of Thermal Hydraulic Design*, Taylor and Francis, 2001.

- [16] C. Chiu, T. E. Neil and W. M. Rohsenow, "Turbulent flow split model and supporting experiments for wire-wrapped core assemblies," *Nuclear Technology*, vol. 50, no. 1, pp. 40-52, 1980.
- [17] S. K. Chen, Y. M. Chen and N. E. Todreas, "The upgraded Cheng and Todreas correlation for pressure drop in hexagonal wire-wrapped rod bundles," *Nuclear Engineering and Design*, vol. 335, pp. 356-373, 2018.
- [18] F. C. Engel, R. A. Markley and A. A. Bishop, "Laminar, transition, and turbulent parallel flow pressure drop across wire-wrap-spaced rod bundles," *Nuclear Science and Engineering*, vol. 69, no. 2, pp. 290-296, 1979.
- [19] K. Rehme, "Pressure drop correlations for fuel element spacers," *Nuclear Technology*, vol. 17, no. 1, pp. 15-23, 1973.
- [20] E. H. Novendstern, "Turbulent flow pressure drop model for fuel rod assemblies utilizing a helical wire-wrap spacer system," *Nuclear Engineering and Design*, vol. 22, pp. 19-27, 1972.
- [21] M.-H. Chun and K.-W. Seo, "An experimental study and assessment of existing friction factor correlations for wire-wrapped fuel assemblies," *Annals of Nuclear Energy*, vol. 28, pp. 1683-1695, 2001.
- [22] E. Bubelis and M. Schikorr, "Review and proposal for best fit of wire-wrapped fuel bundle friction factor and pressure drop predictions using various existing correlations," *Nuclear Engineering and Design*, vol. 238, pp. 3299-3320, 2008.
- [23] S. K. Chen, N. E. Todreas and N. T. Nguyen, "Evaluation of existing correlations for the prediction of pressure drop in wire-wrapped hexagonal array pin bundles," *Nuclear Engineering and Design*, vol. 267, pp. 109-131, 2014.
- [24] S.-K. Cheng, Constitutive correlations for wire-wrapped subchannel analysis under forced and mixed convection conditions, Massachusetts Institute of Technology, 1984.
- [25] S. K. Chen, R. Petroski and N. E. Todreas, "Numerical implementation of the Cheng and Todreas correlation for wire wrapped bundle friction factors - desirable improvements in the transition flow region," *Nuclear Engineering and Design*, vol. 263, pp. 406-410, 2013.
- [26] R. Lyon, "Forced convection heat transfer theory and experiments with liquid metals," ORNL-361, Oak Ridge National Laboratory, 1949.
- [27] R. Lyon, "Liquid metal heat-transfer coefficients," *Chemical Engineering Progress*, vol. 47, no. 2, pp. 75-79, 1951.
- [28] R. C. Martinelli, "Heat transfer to molten metals," *Transactions of the American Society of Mechanical Engineers*, vol. 69, p. 947-959, 1947.
- [29] J. Pacio, L. Marocco and T. Wetzel, "Review of data and correlations for turbulent forced convective heat transfer of liquid metals in pipes," *Heat Mass Transfer*, vol. 51, pp. 153-164, 2015.
- [30] G. L. Hofman, M. C. Billone, J. F. Koenig, J. M. Kramer, J. D. B. Lambert, L. Leibowitz, Y. Orechwa, D. R. Pedersen, D. L. Porter, H. Tsai and A. E. Wright, "Metallic Fuels Handbook," ANL-NSE-3, Argonne National Laboratory, 1989.

- [31] M. Foord, N. Larosa, R. Dennis and E. Courtwright, "ConfigObj," 2014. [Online]. Available: <https://configobj.readthedocs.io/en/latest/>. [Accessed 17 August 2020].
- [32] Reactor Analysis Division, The SAS4A/SASSYS-1 LMR Analysis Code System - Volume 1, ANL-FRA-1996-3, Argonne National Laboratory, 1996.

## Appendix A Pin bundle dimension definitions

Parameter	Definition
$P_{\text{pin}}$	Pin center-to-center pitch distance
$D_{\text{pin}}$	Pin outer diameter
$N_r$	Number of pin rings
$P_{\text{asm}}$	Assembly center-to-center pitch distance
$d_{\text{ff-out}, n}$	Outer flat-to-flat distance of duct wall $n$
$d_{\text{ff-in}, n}$	Inner flat-to-flat distance of duct wall $n$
$N_{\text{wall}}$	Number of duct walls
Pin-to-pin distance	$d_{pp} = P_{\text{pin}} - D_{\text{pin}}$
Pin-to-wall distance	$d_{pw} = \frac{1}{2} [d_{\text{ff-in}, 1} - \sqrt{3} P_{\text{pin}} (N_r - 1) - D_{\text{pin}}]$
Duct wall thickness	$d_{\text{wall}, 1} = \frac{1}{2} (d_{\text{ff-out}, 1} - d_{\text{ff-in}, 1})$
Bypass gap width	$d_{\text{byp}} = \frac{1}{2} [d_{\text{ff-in}, 2} - d_{\text{ff-out}, 1}]$
Inter-assembly gap width	$d_{\text{gap}} = P_{\text{asm}} - d_{\text{ff-out}, N}$
Interior-interior subchannel distance	$L_{11} = \frac{\sqrt{3}}{3} P_{\text{pin}}$

Interior-edge subchannel distance	$L_{12} = \frac{\sqrt{3}}{6} P_{\text{pin}} + \frac{1}{2} \left( \frac{1}{2} D_{\text{pin}} + d_{\text{pin-wall}} \right)$
Edge-edge subchannel distance	$L_{22} = P_{\text{pin}}$
Edge-corner subchannel distance	$L_{23} = \frac{1}{2} \left( P_{\text{pin}} + \frac{1}{\sqrt{3}} \left( \frac{1}{2} D_{\text{pin}} + d_{\text{pin-wall}} \right) \right)$
Corner-corner subchannel distance	$L_{33} = \frac{1}{\sqrt{3}} (D_{\text{pin}} + d_{\text{pin-wall}})$
First duct wall interior corner length	$c_{\text{w-in},1} = \frac{1}{\sqrt{3}} \left( \frac{D_{\text{pin}}}{2} + d_{\text{pin-wall}} \right)$
First duct wall exterior corner length	$c_{\text{w-out},1} = \frac{1}{\sqrt{3}} \left( \frac{D_{\text{pin}}}{2} + d_{\text{pin-wall}} + d_{\text{wall},1} \right)$
Second duct wall interior corner length	$c_{\text{w-in},2} = \frac{1}{\sqrt{3}} \left( \frac{D_{\text{pin}}}{2} + d_{\text{pin-wall}} + d_{\text{wall},1} + d_{\text{bypass}} \right)$
Second duct wall exterior corner length	$c_{\text{w-out},2} = \frac{1}{\sqrt{3}} \left( \frac{D_{\text{pin}}}{2} + d_{\text{pin-wall}} + d_{\text{wall},1} + d_{\text{bypass}} + d_{\text{wall},2} \right)$



This page left blank intentionally





**Nuclear Engineering Division**

Argonne National Laboratory  
9700 South Cass Avenue, Bldg. 208  
Argonne, IL 60439

[www.anl.gov](http://www.anl.gov)



Argonne National Laboratory is a U.S. Department of Energy  
laboratory managed by UChicago Argonne, LLC